Tutkimusraportti 46
Research Report 46

Multibody Simulation Model of the Roller Test Rig

Jussi Sopanen

ISBN 951-764-837-5
ISSN 1459-2932

Department of Mechanical Engineering
Lappeenranta University of Technology
P.O. Box 20
FIN-53851 Lappeenranta
Finland

Lappeenranta, November, 2003

ABSTRACT

Multibody simulation model of the roller test rig is presented in this work. The roller test rig consists of a paper machine's tube roll supported with a hard bearing type balancing machine. The simulation model includes non-idealities that are measured from the physical structure. These non-idealities are the shell thickness variation of the roll and roundness errors of the shafts of the roll. These kinds of non-idealities are harmful since they can cause subharmonic resonances of the rotor system. In this case, the natural vibration mode of the rotor is excited when the rotation speed is a fraction of the natural frequency of the system. With the simulation model, the half critical resonance is studied in detail and a sensitivity analysis is performed by simulating several analyses with slightly different input parameters. The model is verified by comparing the simulation results with those obtained by measuring the real structure. Comparison shows that good accuracy is achieved, since equivalent responses are achieved within the error limit of the input parameters.

Keywords: tube roll, multibody simulation, subharmonic vibrations.

Table of Contents

1 INTRODUCTION

This work report summarizes the ADAMS simulation model of the roller test rig used in the PyöriVÄRE project. The studied structure is a tube roll of a paper machine, which is located at the laboratory of Machine Design at Helsinki University of Technology. The tube roll is supported with a hard bearing type balancing machine. The purpose of this report is to describe all the important properties of the ADAMS simulation model. Modeling assumptions and the theory behind various calculations are presented. Simulation results are compared to those obtained by measurement from the existing roll.

The half critical resonance is studied in detail. After comparison to measurements, a sensitivity analysis is performed by simulating several analyses with slightly different parameters. These parameters are the amplitudes and phase angles of the 2nd order waviness of the shaft of the roll, bending stiffness variation of the roll and modal damping ratio of the first vertical bending mode.

The ADAMS simulation model of the roller test rig is shown in Figure 1. The model contains 5 flexible parts and 7 rigid parts. Parts are connected with constraints, spring-damper forces and contact forces. The used ADAMS version is 10.0.

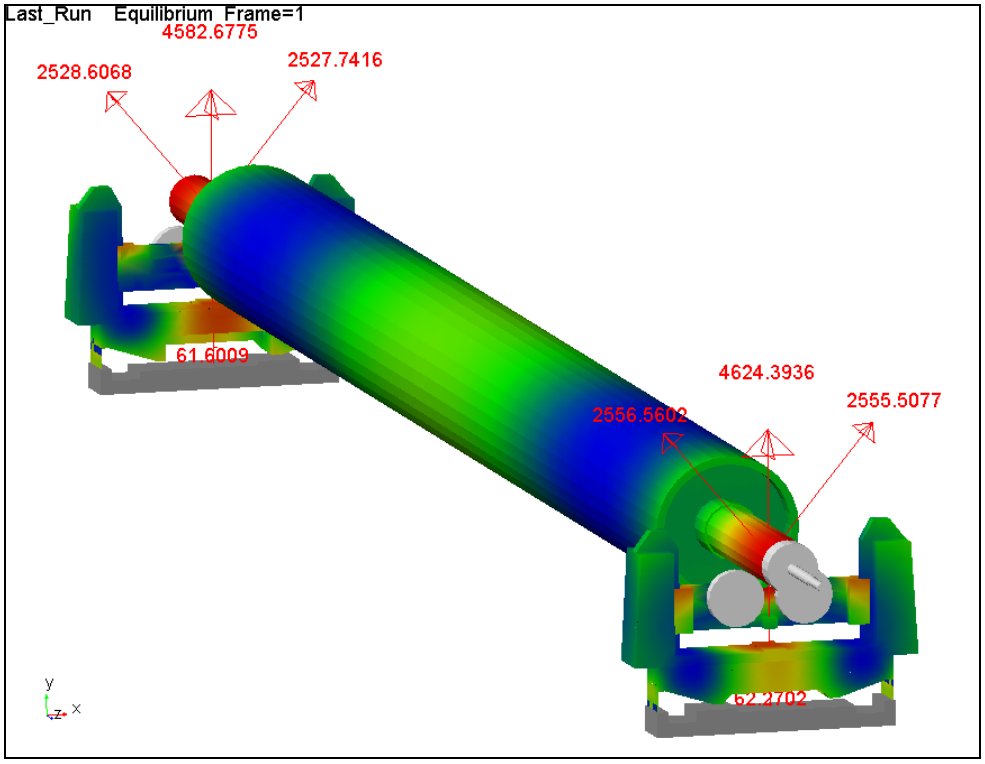

Figure 1. The ADAMS simulation model of the roller test rig.

This report is organized as follows: In chapter 2 the modeling of the flexible parts is reported. The flexibility of the parts is imported from FE-models to ADAMS. Chapter 3 deals with contact forces between the roll and the pedestal of the balancing machine and waviness of the shaft and support rollers. The assembled model and optimization of the modal parameters are discussed in chapter 4. In chapter 5, the simulation results are compared to measurements and the effect of variation in the initial parameters to half-critical vibration response is studied. The comparison shows that excellent agreement between the simulated and measured results is obtained. In chapter 6, few additional simulations are performed. Modeling aspects, such as mode selection of the flexible bodies and inertia modeling of the roll, are studied in these simulations.

2 FLEXIBLE BODIES

Structural flexibility of the flexible parts is imported from detailed FE-models to the dynamics simulation model. The simulation model contains five flexible parts, but only three different kinds of parts. These are: *the roll, the steel plate* and *the frame*.

2.1 The roll

Geometry of the modeled paper machine's tube roll is shown in Figure 2. The roll is made of steel by welding and turning. The coordinate system of the roll is shown in Figure 3. This coordinate system is used in the FE-model as well as in the ADAMS model.

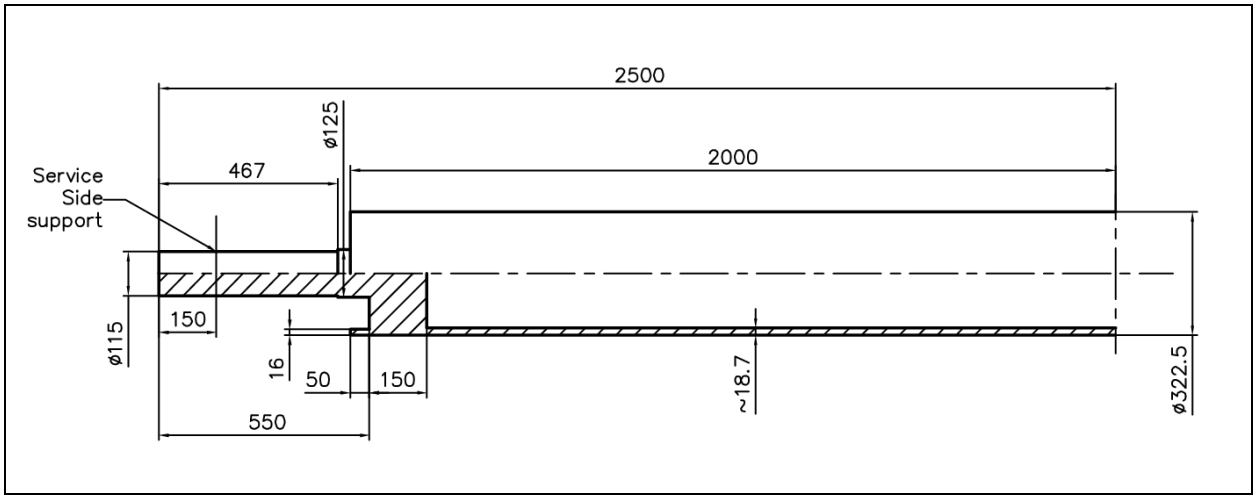

Figure 2. Geometry of the roll. The roll is symmetric.

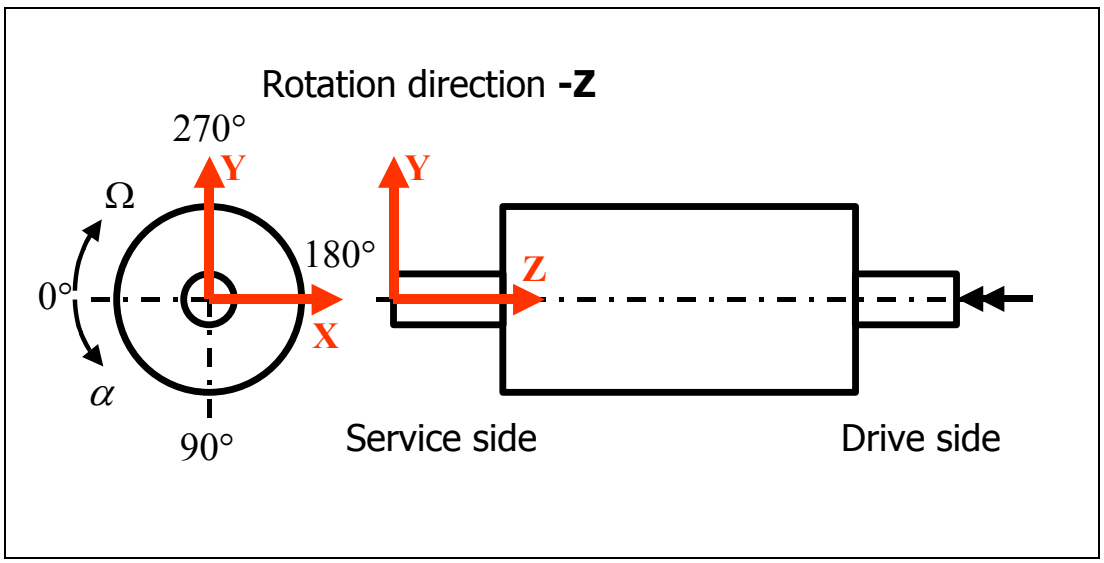

Figure 3. The right-handed coordinate system is at the service side end of the roll and the attitude angle α increases counterclockwise. Rotation direction is negative around Z-axis.

2.1.1 FE-model of the roll

The FE-model of the roll (Figure 4) is created by using ANSYS 5.5 finite element software. Since the ADAMS implementation of Craig-Bampton substructuring technique uses lumped masses, a detailed solid element mesh is created. By using a dense finite element mesh, approximately correct rotational inertias are obtained. The roll is modeled using 8-node brick shaped solid elements with rotational degrees-of-freedom (SOLID73). The element type SOLID73 is degenerated from 20-node solid element by condensing out the motions of the midside nodes and then converting them to rotational motions of the corner nodes [2]. The properties of the FE-model are shown in Table 1. The bearing locations of the roll are stiffened by using stiff and low mass beam elements (BEAM4), whose Young's modulus is 2.07E+13 N/m^2 and the mass density is 0.7801 kg/m^3. In ADAMS, the bearing forces are applied to only one node and thus unstiffened solid element mesh would give corrupted results.

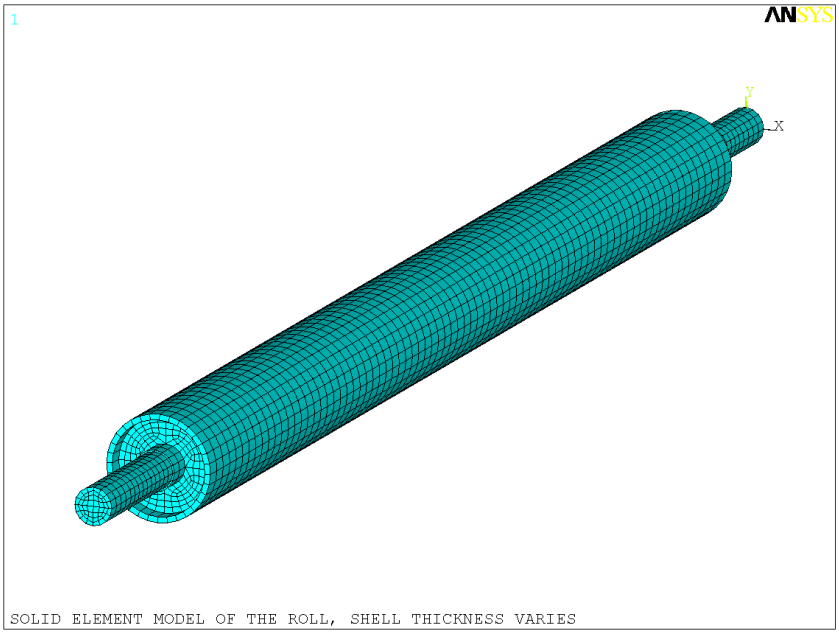

Figure 4. The FE-model of the studied roll.

Table 1. Properties of the FE-model of the roll.

Number of nodes	8744
Number of elements	5536
Material Properties:	
Young's Modulus	2.07E+011 N/m^2
Mass Density	7801 kg/m^3
Poisson's Ratio	0.3

In the FE-model the thickness of the shell is in accordance with the measured results and because of that the mass and stiffness distribution of the roll is taken into account in the simulation model. This non-ideality causes a so-called weight resonance, which means that stiffness variation excitates symmetrical modes. This resonance occurs when the rotating speed is one half of the symmetrical critical speed.

The variation of the shell thickness in paper machine's tube rolls is, in general, in the inner surface of the shell. Usually the outer surface of the roll is manufactured accurately. This is also

true in the case of the studied roll, as can be seen from the initial curvature measurement of the roll [1]. Figure 5 shows the shape of the outer surface at different attitude angles. The only significant form error in the outer surface is crowning. This crowning is modeled in the FE-model by moving nodes at the outer surface of the roll.

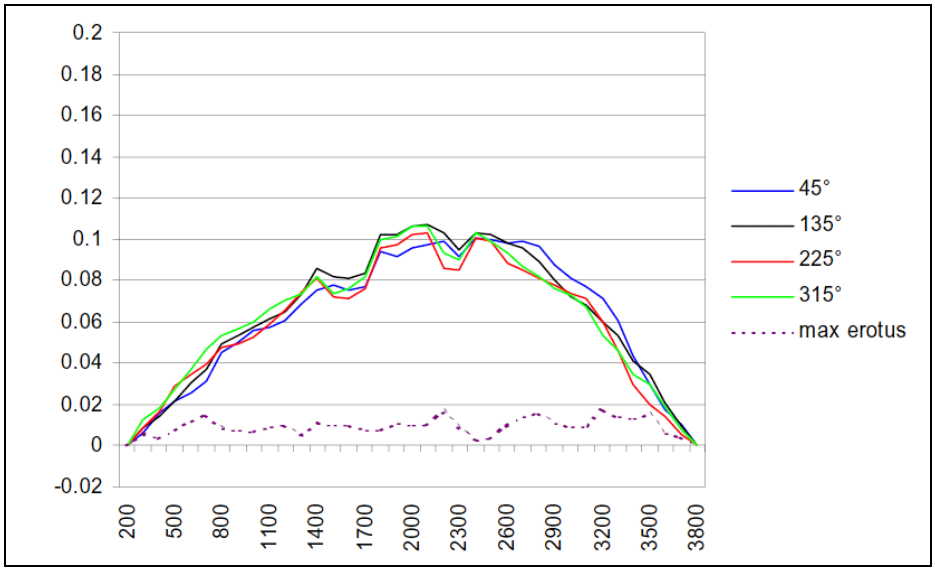

Figure 5. Results of the outer surface measurement of the test roll [1]. Dashed line is the maximum difference between measurements.

The shell thickness of the roll is measured in 740 points. The number of evenly distributed measurement points in circumferential direction is 20 and in longitudinal direction 37, respectively. The measured shell thickness is shown in Figure 6. The used finite element mesh is not the same size as the grid used in the measurement. Because of that, a cubic interpolation method is used to obtain the shell thickness at the nodal points (Figure 7). The procedure of modeling the non-ideal roll is shown in Figure 8 as a flow chart.

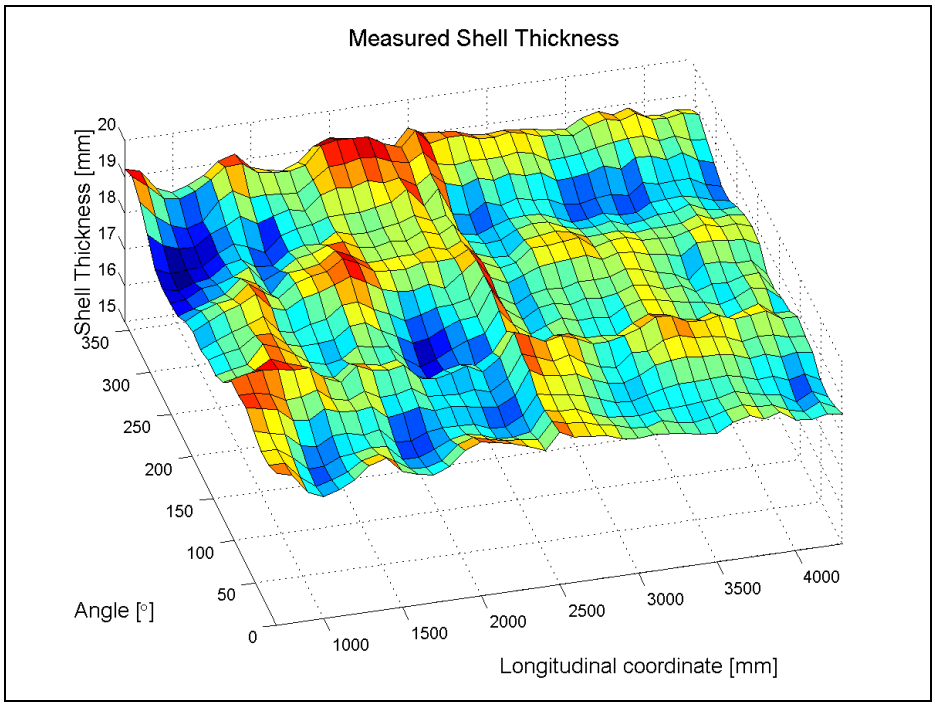

Figure 6. The measured shell thickness map. Thickness varies between 17.86 – 19.59 mm, an average value is 18.72 mm.

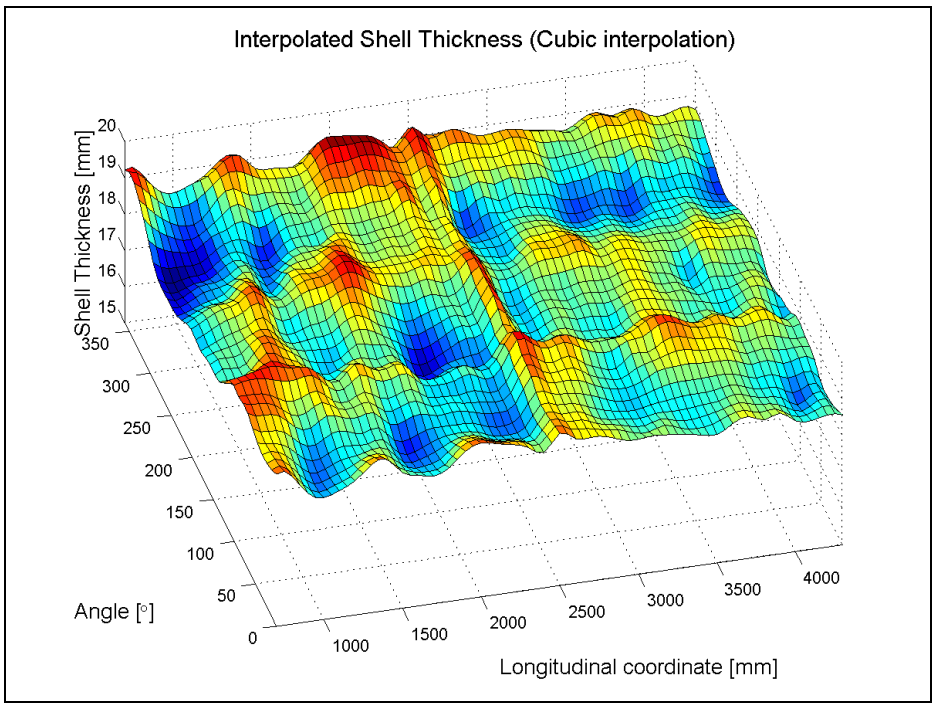

Figure 7. The interpolated shell thickness map.

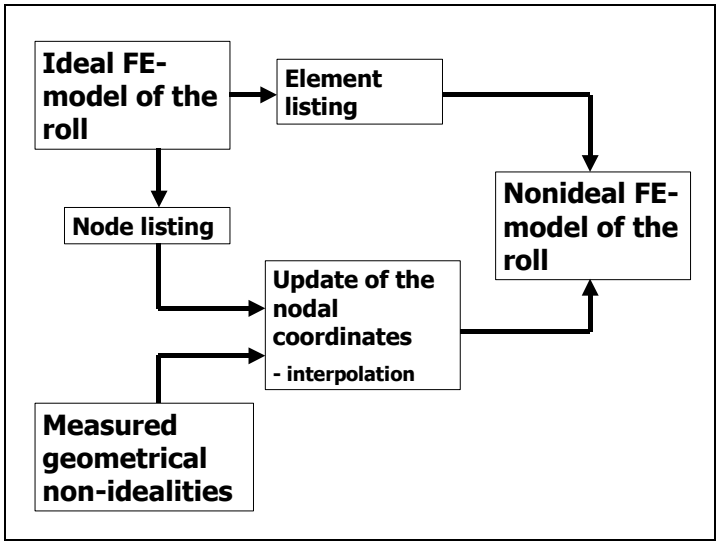

Figure 8. The procedure of modeling the non-ideal roll.

2.1.2 Solved modes and selection

By using a technique described in the references [3, 4, 5], the Craig-Bampton modes are solved. At first, a total of 56 fixed interface modes and 12 static correction modes are extracted from the FE-model of the roll. This set of modes is then orthonormalized and a set of approximate free-free modes and boundary modes is obtained. The quality of the final set of modes depends on the quality of the first set. If the first set is corrupted, the final set is also corrupted. Furthermore, the use of lumped mass formulation decreases the accuracy of the solution. Due to these facts, the quality of the approximate free-free modes is investigated by solving free-free modes directly from the full FE-model. Comparison between the natural frequencies of the free-free modes is shown in Table 2. It can be seen that the accuracy of the solution is excellent.

Table 2. Comparison between the 20 lowest orthonormalized Craig-Bampton frequencies and the frequencies solved from the full FE-model.

Mode	Craig-Bampton Freq. [Hz]	Lumped Mass Freq. [Hz]	Difference	Consistent Mass Freq. [Hz]	Difference
7	77,76	77,75	-0,01 %	77,79	0,04 %
8	77,90	77,90	-0,01 %	77,93	0,04 %
9	199,95	199,76	-0,10 %	199,98	0,01 %
10	200,17	199,98	-0,10 %	200,19	0,01 %
11	279,64	278,79	-0,30 %	279,26	-0,13 %
12	279,74	278,89	-0,30 %	279,36	-0,13 %
13	348,53	347,78	-0,21 %	348,39	-0,04 %
14	348,65	347,91	-0,21 %	348,52	-0,04 %
15	354,49	354,46	-0,01 %	356,33	0,52 %
16	464,54	463,85	-0,15 %	463,88	-0,14 %
17	523,26	522,89	-0,07 %	523,86	0,11 %
18	523,54	523,17	-0,07 %	524,14	0,11 %
19	545,60	545,60	0,00 %	545,85	0,05 %
20	546,17	546,17	0,00 %	546,42	0,05 %

For the dynamic analysis a set of bending and longitudinal modes is selected. Torsion modes as well as shell vibration modes i.e. local vibration modes are disabled. The mass properties and selected modes and their frequencies are shown in Table 3. The non-ideality of the roll can be seen from the mass properties and from the natural frequencies of the roll. The location of the center of mass is not in the neutral axis and the cross products of inertia are not equal to zero. The frequencies of the bending mode pairs are not equal as they would be in the case of ideal roll.

During operation the roll is subjected to high inertia forces and thus all nine mass inertia invariants are used in the simulation.

Table 3. Mass properties and selected modes of the roll.

Mass Properties of the Roll			**Selected modes of the Roll** Number of Selected Modes: 24			
Mass [kg]:	791.11		Mode	Freq. [Hz]	Mode	Freq. [Hz]
			7	77.76	29	779.04
Center of mass (relative to service side end)			8	77.90	34	982.45
X [mm]	Y [mm]	Z [mm]	9	199.95	35	1054.41
-0.010	-0.053	2499.705	10	200.17	36	1054.60
			11	279.64	42	1301.37
Inertia tensor [kgm^2]			12	279.74	43	1301.65
			13	348.53	44	1460.24
6649.988	0.005	0.024	14	348.65	45	1460.94
	6650.008	0.070	16	464.54	57	1595.25
symm.		14.525	17	523.26	58	1596.37
			18	523.54	65	11941.95
			28	778.75	66	11982.07

As mentioned before, the shell thickness variation of the roll leads to the so-called weight resonance. In order to study the effect of stiffness variation to the half critical resonance, the shell thickness variation is doubled and corresponding modes are solved. The thickness of the shell at node *i* is calculated as follows:

$$t_{i\_2x} = t_{mean} + 2 \cdot (t_i - t_{mean}) \tag{2.1}$$

where t_{mean} is an average shell thickness and t_i is the original thickness at the node *i*. The resulted mass properties and selected modes are shown in Table 4 below.

Table 4. Mass properties and selected modes of the roll, when shell thickness variation is two-fold.

Mass Properties of the Roll			**Selected modes of the Roll** Number of Selected Modes: 24			
Mass [kg]: 791.18			Mode	Freq. [Hz]	Mode	Freq. [Hz]
			7	77.69	29	779.09
Center of mass (relative to service side end)			8	77.97	34	981.13
X [mm]	Y [mm]	Z [mm]	9	199.80	35	1053.66
-0.019	-0.106	2499.416	10	200.24	36	1054.04
			11	279.54	42	1301.17
Inertia tensor [kgm^2]			12	279.74	43	1301.70
			13	348.43	44	1457.36
6648.110	0.010	0.047	14	348.68	45	1459.85
	6648.149	0.141	16	464.82	57	1594.53
symm.		14.526	17	522.83	58	1596.75
			18	523.40	65	11886.71
			28	778.48	66	11965.07

2.1.3 Comparison with the Experimental Modal Analysis

The natural frequencies of the test roll were measured with experimental modal analysis [6]. The roll was lifted up with lifting belts and a flexible spring set. The measured rigid body modes were very near to zero. The results of the experimental modal analysis are shown in Table 5. Incorrect damping ratios for modes 2, 3 and 6 are due to lifting belts, which increased damping in vertical direction. Because of that, lower damping value is used for each mode pair. Only frequencies are determined from the Frequency Response Function (FRF) for modes 7-14, the modes and damping ratios were not measured

Table 5. The results of the rolls modal analysis.

Mode	Freq. [Hz]	ζ [%]	Comments
1	78.048	0.018	
2	78.285	0.138	Damping incorrect
3	196.67	0.035	Damping incorrect
4	196.93	0.016	
5	270.27	0.023	
6	270.35	0.034	Damping incorrect
7	342.6	-	Vertical FRF
8	342.5	-	Horizontal FRF
9	525.6	-	Vertical FRF
10	523.9	-	Horizontal FRF
11	784.2	-	Vertical FRF
12	784.4	-	Horizontal FRF
13	1059	-	Vertical FRF
14	1059	-	Horizontal FRF

Because the roll is non-ideal, the frequencies of two similar bending modes are not equal. When presented in the XY-plane these bending modes are approximately perpendicular to each other.

Comparison between the measured modes and those obtained from model is shown in Figure 9. It can be seen that the directions of the two lowest bending modes differ. This indicates that the lowest and the highest bending stiffnesses are not in the same attitude angle in the model and in the real roll. Discrepancies in direction can be also seen from other two bending mode pairs.

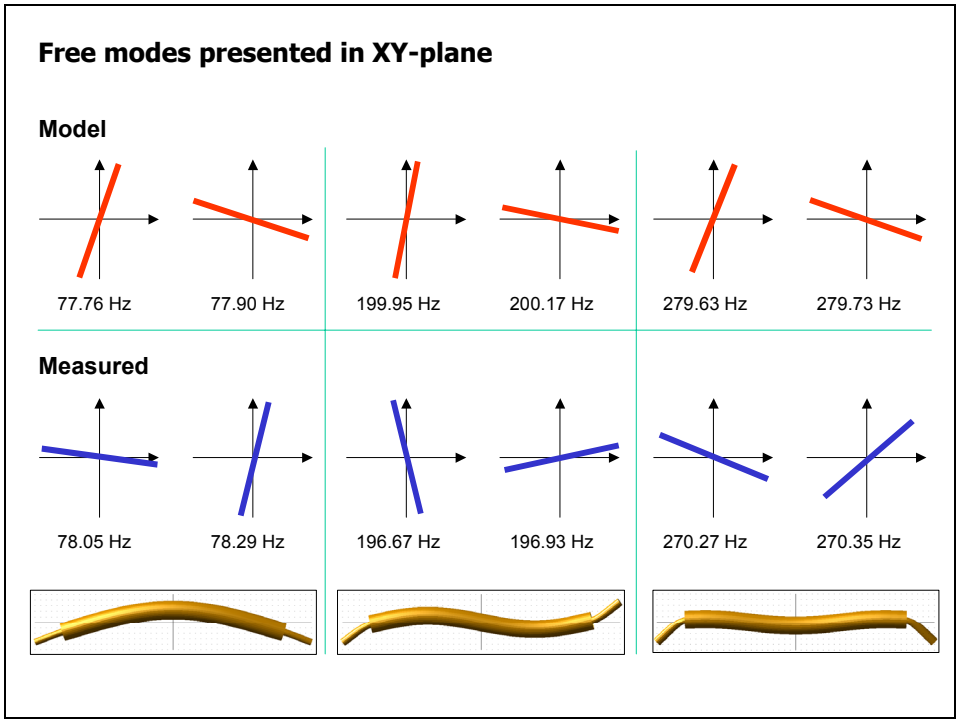

Figure 9. Comparison between the measured and calculated modes of the roll.

Due to non-ideality, the roll has minimum and maximum bending stiffnesses. This stiffness variation is not measured from the real roll, but it can be estimated from two lowest frequencies. If we assume that the vibrating mass of the roll is constant and bending stiffness is directly proportional to the square of bending mode frequency, we can calculate percentage stiffness variation as follows

$$\left(1-\frac{k_{\min}}{k_{\max}}\right)\cdot 100\% = \left(1-\left(\frac{f_{\min}}{f_{\max}}\right)^2\right)\cdot 100\% \qquad (2.2)$$

The approximate stiffness variations of different rolls are:

- Model, normal thickness variation 0.36 %
- Model, two-fold thickness variation 0.73 %
- Measured from the real roll 0.60 %.

It seems that the real roll has larger stiffness variation than the model with normal thickness variation. Model with two-fold thickness variation is nearer to measured result. The real roll has other non-idealities than shell thickness variation, such as welds and uneven modulus of elasticity. It must be pointed out that this calculation method is not accurate, but it gives an approximation of the stiffness variation.

Bending stiffness variation can be measured from the FE-model of the roll. A force of 5000 N is applied at the middle of the roll and all displacements as well as rotation around Z-axis are constrained at bearing nodes. Force direction rotates full circle by 2 degree increments. The following results are obtained:

Normal shell thickness variation:

- Minimum Bending Stiffness = 17.163 MN/m^2 @ 74°
- Maximum Bending Stiffness = 17.220 MN/m^2 @ 164°
- Variation percentage = 0.33 %

Two-fold variation:

- Minimum Bending Stiffness = 17.147 MN/m^2 @ 76°
- Maximum Bending Stiffness = 17.262 MN/m^2 @ 166°
- Variation percentage = 0.67 %

These values corresponds well with those calculated from frequencies.

2.2 Other flexible parts

The pedestal of the balancing machine is modeled with two flexible parts and three rigid bodies as shown in Figure 10. Modeling of the flexible parts *steel plate* and *frame* is described in detail in the following sections.

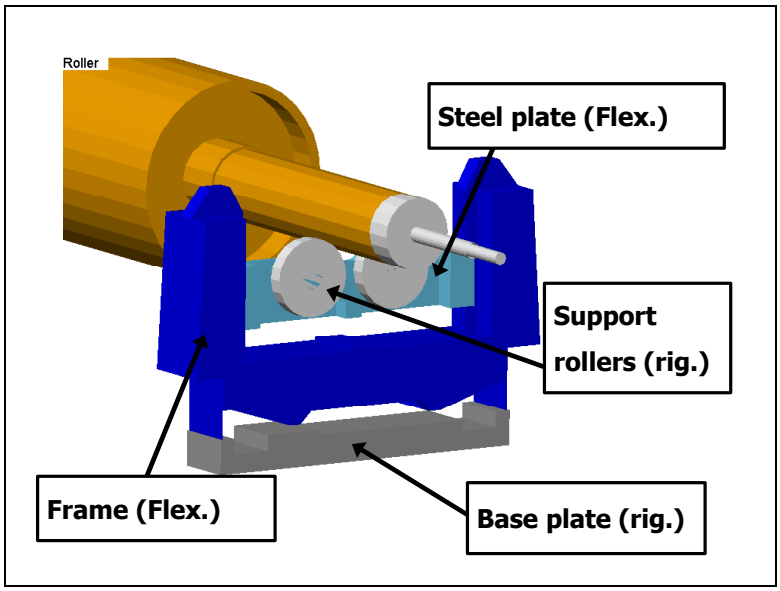

Figure 10. Parts in the pedestal of the balancing machine.

2.2.1 The steel plate

In the real balancing machines pedestal, the support rollers are connected to the steel plate with needle roller bearings. The steel plate carries all bearing loads and therefore its flexibility is important to take into account. The FE-model of the steel plate is shown in Figure 11 and model properties are listed in Table 6. The used element type is SOLID73. The attachment locations are stiffened by using stiff beam elements (BEAM4) and by using constraint equations. A total of 5 attachment nodes are defined. A total of 36 fixed interface modes and 30 static correction modes are extracted from the FE-model.

Table 6. Properties of the FE-model of the steel plate.

Number of nodes	1404
Number of elements	812
Calculated Mass	6.47 kg
Material Properties:	
Young's Modulus	2.10E+011 N/m^2
Mass Density	7801 kg/m^3
Poisson's Ratio	0.3

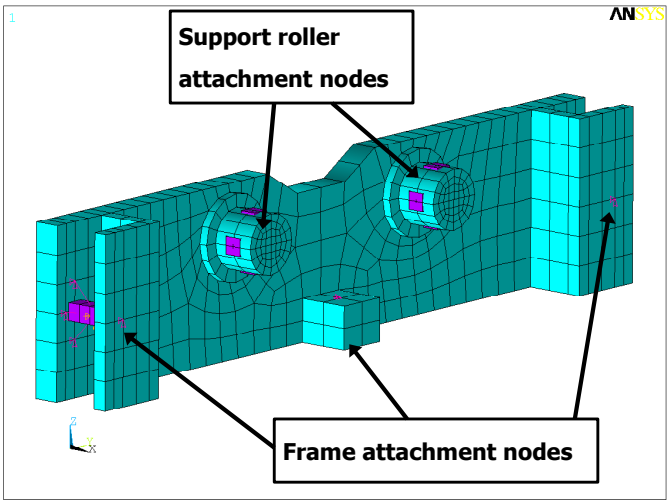

Figure 11. The FE-model of the steel plate.

2.2.2 The Frame

The frame part is an assembly of a base part made of cast iron and steel parts, which are bolted to the base part. The attachment locations are stiffened by using constraint equations. The used element types are SOLID73, SHELL63 and BEAM4. A total of 36 fixed interface modes and 36 static correction modes are extracted from the FE-model. The FE-model of the frame is shown in Figure 12 and model properties are listed in Table 7.

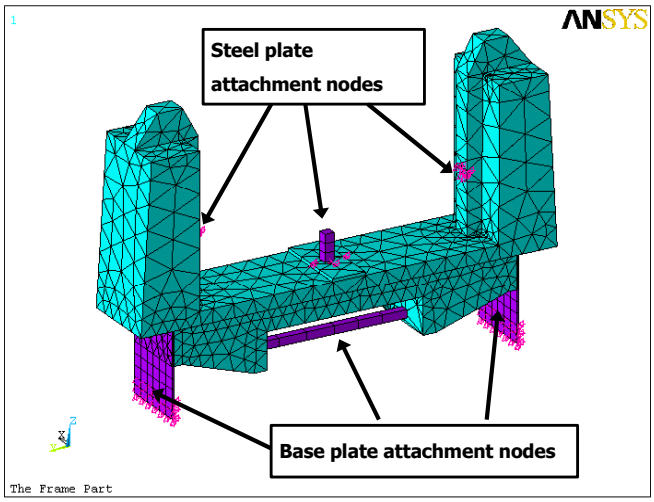

Figure 12. The FE-model of the frame part. Steel parts (purple) are bolted to cast iron (cyan) base part.

Table 7. Properties of the FE-model of the frame.

Number of nodes	1816	
Number of elements	5403	
Material Properties:	Cast iron	Steel
Young's Modulus	1.00E+011 N/m^2	2.10E+011 N/m^2
Mass Density	7080 kg/m^3	7801 kg/m^3
Poisson's Ratio	0.221	0.3
Calculated Mass	40.96 kg	

2.2.3 Mode selection of the frame and the steel plate

The selection of the modes of two flexible parts in the pedestal is based on the strain energy of the modes. Since orthogonal modes are used it is possible to calculate the strain energy contribution of the individual modes to the total strain energy [8]. Selection of vibration modes is done by simulating a typical analysis with all modes selected. After that the modes, which contribute more than 0.1 % to the total strain energy, are selected. Selected modes and their natural frequencies are shown in Table 8.

Table 8. The selected modes of the steel plate and the frame.

Steel Plate 24 Selected Modes				**Frame** 34 Selected Modes					
Mode	Freq. [Hz]	Mode	Freq. [Hz]	Mode	Freq. [Hz]	Mode	Freq. [Hz]	Mode	Freq. [Hz]
7	349	22	6762	8	229	34	3311	52	7151
9	966	26	7152	9	419	35	3420	53	7443
10	1609	32	9071	12	683	36	3636	55	8184
11	1754	34	9721	13	891	37	3667	56	11065
12	2041	35	10287	15	994	39	3712	57	11753
13	2701	39	11575	17	1081	40	3713	58	12480
14	2827	44	13632	23	2048	42	4293	59	14186
15	3814	46	14400	28	2896	45	5209	68	32181
16	4318	48	16918	29	2932	47	5560	69	33272
17	4505	52	20580	30	2972	48	5627	70	34608
19	5373	54	21470	31	3058	49	5688		
20	6250	62	43876	33	3232	50	5779		

It can be seen from the natural frequencies that both flexible parts in the pedestal assembly are quite stiff. The deformations are not expected to be large in these parts. Because of that, the mass matrices of the steel plate and the frame are selected to be constant during simulation. High frequency modes are boundary modes i.e. static correction modes after orthonormalization. Dynamics of these modes are excluded by defining their damping ratio as 100 %, which means critical modal damping. However, contribution of these modes to the deformation of the parts is included.

3 CONTACT FORCES BETWEEN ROLL AND PEDESTAL

The contact forces between the shaft and the pedestal are described in this chapter. These forces are important, because waviness of the shafts causes excitations to the roll. These excitations contain harmonic components, which are multiples of the rotation speed. Waviness of the shaft is thus the main reason to the so-called sub-harmonic resonances. Firstly, the calculation of the contact force parameters is described. Second part of this chapter deals with the modeling of the shafts and support roller waviness.

3.1 Contact force between shaft and support rollers

The roll is supported by two rollers in the balancing test rig (Figure 13). Simple springs or constraints cannot be used to model this kind of support, because the roll can lift off freely. That is why contact forces are defined between the roll and the support rollers. These forces are important to model accurately, because the sub-harmonic vibration excitations come mainly from them. The contact force is a function of contact penetration and penetration velocity according to the equation (3.1) [8].

$$F = \begin{cases} k_i\,(x_1 - x)^e - STEP(x, x_1 - d, c_{\max}, x_1, 0)\cdot \dot{x} & , x < x_1 \\ 0 & , x \geq x_1 \end{cases} \tag{3.1}$$

where k_i is the spring constant, x_1 is the contact distance and x is the distance between contacting bodies. A STEP-function is used to obtain a continuous contact force. A parameter d is the penetration, when the maximum damping constant $c_{\max}$ is achieved. As shown in Figure 13, the support rollers are connected to the steel plate by needle roller bearings. In order to calculate the stiffness coeffient k_i, the flexibility of the roll-support roller contact as well as the flexibility of the needle roller bearing must be taken into account. These two non-linear springs are connected as series.

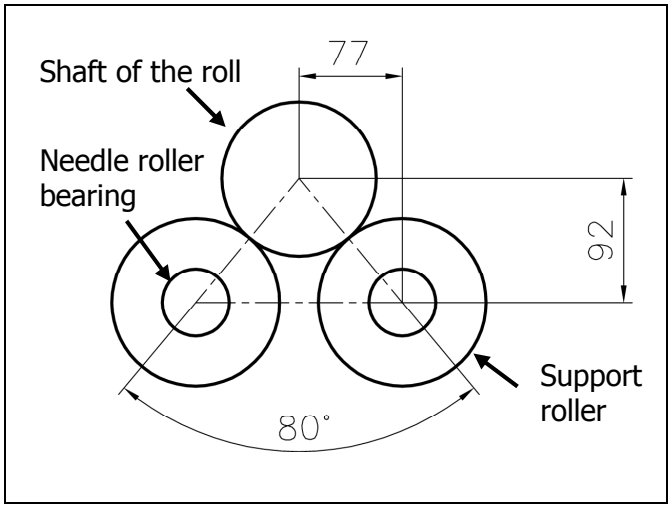

Figure 13. Support rollers and shaft of the roll.

The first contact is between the shaft and the support roller. This problem can be solved using Hertzian theory related to the contact between elastic solids [7]. In this case the type of contact is cylinder-cylinder and the contact area is rectangular. The force-deflection relationship can be solved from equations (3.2) and (3.3)

$$b = \sqrt{\frac{4 \cdot F}{\pi L_1} \cdot \frac{(1-\nu^2)}{E} \cdot \left(\frac{1}{D_1} + \frac{1}{D_2} \right)^{-1}}, \tag{3.2}$$

where b is the semiwidth of the contact, F is the force, L_1 is the length of the cylinder, ν and E are the Poisson's ratio and the modulus of elasticity of the material and D_1 and D_2 are the diameters of the cylinders. The total deflection between the cylinders is:

$$\delta_{cc} = \frac{2(1-\nu^2)F}{\pi L_1 E} \cdot \left(\frac{2}{3} + \ln \frac{4 D_1 D_2}{b^2} \right). \tag{3.3}$$

The second contact is between the support roller and needle roller bearing. The stiffness of the needle roller bearing can be calculated as described by Eschmann [9]. In a needle roller bearing, the total load is carried by contact forces between needles and races. The number of contacting needles depends on the diametral play of the bearing and deformation. The load-carrying angle can be calculated as

$$\psi = 2\cos^{-1}\left(\frac{c_d}{2\delta_r} \right), \tag{3.4}$$

where c_d is the diametral play and δ_r is the displacement in radial direction. It can be seen from the above equation that the load-carrying angle is 180°, when the diametral play is zero.

The stiffness coefficient for the contact between one needle and both inner and outer race of the bearing can be calculated from equation (3.5) [9]

$$k_{needle} = 26200 \cdot l_r^{0.92}, \tag{3.5}$$

where l_r is the length of the roller. The elastic deformation in needle i is calculated from the radial displacement δ_r between the inner and the outer race (Figure 14) as follows

$$\delta_i = \delta_r \cdot \cos\phi_i - \frac{c_d}{2}, \tag{3.6}$$

where ϕ_i is the attitude angle of the needle i. The total force of the needle roller bearing can be calculated from the following equation

$$F_{nr} = \sum_{i=1}^{z} k_{needle} \delta_i^{1.08} \cos\phi_i, \tag{3.7}$$

where summation includes only those needles in which δ_i is greater than zero.

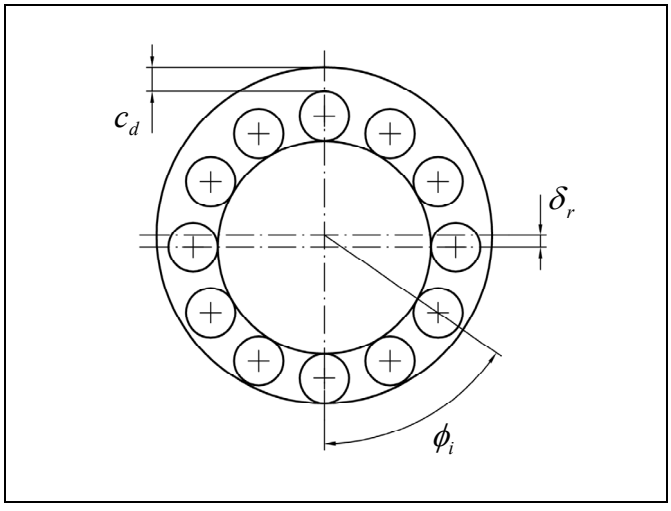

Figure 14. Schematic picture of the needle roller bearing.

Both above-mentioned contacts have nonlinear force-displacement relationships. The force-deflection relationship between two cylinders can be solved for a given force without iteration, while corresponding relationship for needle roller bearing can be solved for given displacement. This fact causes difficulties when combining these two stiffnesses. Therefore, both force-deflection relationships are first calculated in Matlab program. Resulted data series are fitted by least squares method to the power equation $F = k\delta^e$. The results of the fitting procedure are shown in Figure 15 and the numerical values used in calculation are shown in Table 9.

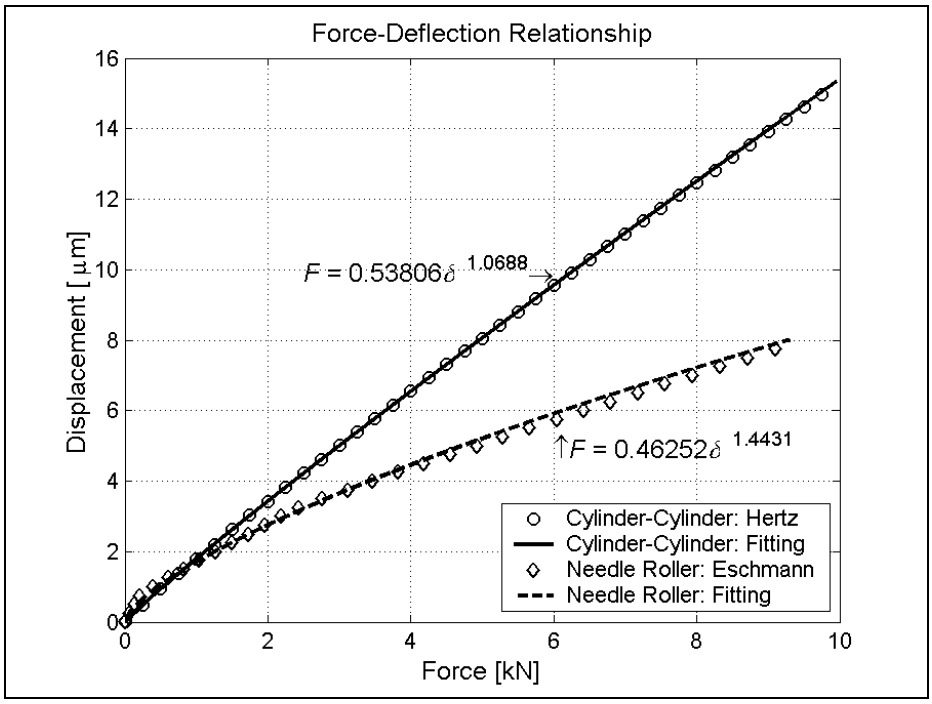

Figure 15. The force-deflection relationships of the cylinder-cylinder contact and the needle roller bearing.

Table 9. Numerical values used in contact parameter calculation.

Cylinder-Cylinder contact		**Needle Roller Bearing**	
Length L_1	25.0 mm	Length of the needle l_r	24.0 mm
Diameter D_1	115.0 mm	Diametral play c_d	50.0 µm
Diameter D_2	125.0 mm	Number of needles z	26
Materials properties:			
Young's Modulus	206000 N/mm^2		
Poisson's Ratio	0.3		

The total deformation can be calculated by using the fitted coefficients as follows

$$\Delta_{tot} = \left(\frac{F}{k_{cc}}\right)^{\frac{1}{e_{cc}}} + \left(\frac{F}{k_{nr}}\right)^{\frac{1}{e_{nr}}} \tag{3.8}$$

where subscripts *cc* and *nr* refers to cylinder-cylinder contact and needle roller bearing, respectively. To obtain the final stiffness coefficient k_i and the exponent for force-deflection relationship e, the points obtained from equation (3.8) are once again fitted. The resulted values are

- $k_i = 0.2146\ kN/\mu m^{1.2173}$
- $e = 1.2173$.

The fitting result is very good as can be seen from Figure 16, where calculated and fitted points are plotted. Damping in rolling element bearings is usually negligible. According to Krämer [10], the damping of rolling element bearing is

$$c = (0.25...2.5)\cdot 10^{-5}\, k_i \left(\frac{Ns}{\mu m} \right), \tag{3.9}$$

where k_i is in $N/\mu m$. Thus the contact damping coefficient is selected to be $c_{max} = 2.5 \cdot 10^{-5} \cdot k_i$. The penetration depth d is selected to be 5.0 μm, which is approximately the penetration in the static equilibrium.

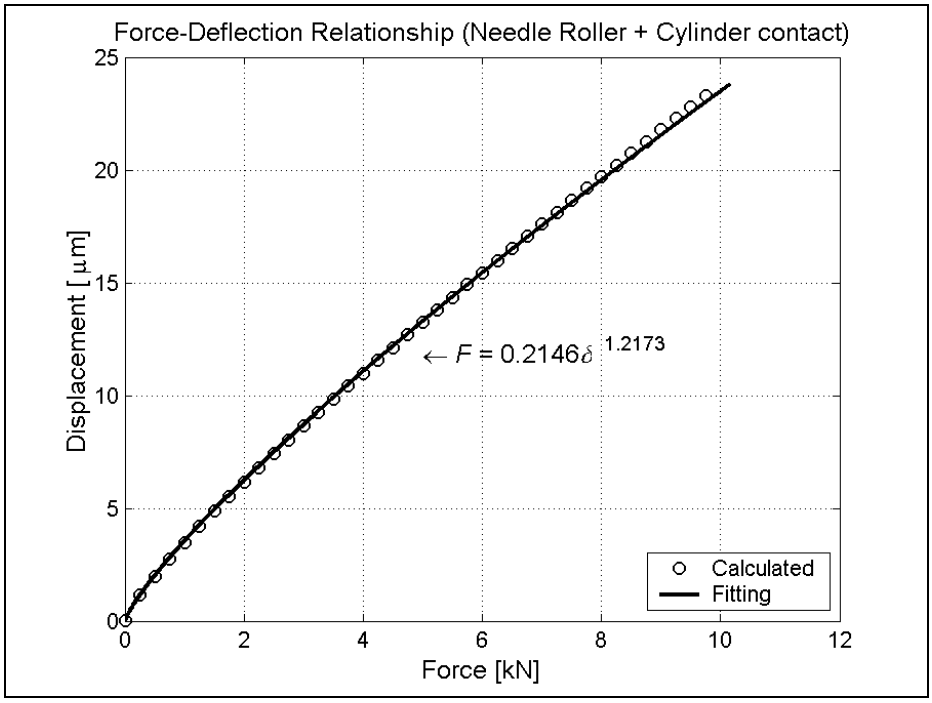

Figure 16. The combined force-deflection relationship.

3.2 Modeling of shafts and support rollers' waviness

The measured roundness profiles of shaft necks and support rollers are analyzed with FFT. As a result the amplitudes and phase angles of the harmonic components are obtained. The roundness profile can be presented as Fourier cosine series by using equation (3.10).

$$R(\alpha) = \sum_{k=1}^{n} c_k \cos\left(k \cdot \alpha + \phi_k\right), \tag{3.10}$$

where c_k is the amplitude and ϕ_k is the phase angle of the k^{th} harmonics and α is the attitude angle of the roll. In the simulation model attention is paid to the harmonic components of only 1^{st} - 4^{th} order because the amplitudes of higher components are insignificantly small.

The roundness errors of the support rollers are distinctly smaller than those of the shafts necks. Furthermore, the impulses, which come from them, are not repeated similarly on every rotation of the roll because the diameter of the shaft necks is 125 mm and the diameter of the support rollers is 115 mm. It is not possible to model the throw of the support rollers exactly because there may be differences of the amount of one tenth millimetre in the diameters of the rollers. In that case the rotation angle of one support roller will not change in the same relation with other support rollers and the rotation angle of the roll. Therefore it is decided to model the roundness error of the support rollers without the phase angles. The measuring accuracy of the roundness is ± 1 μm for the shaft and ± 0.2 μm for the support rollers. The error estimate for the phase angles

of the harmonic components is ± 20 degrees. The waviness of the shaft is shown graphically in Figure 17.

Table 10. The measured roundness errors of the rolls shaft and support rollers.

SHAFT OF THE ROLL					
Drive Side			**Service Side**		
k	Amplitude c_k [μm]	Phase ϕ_k [rad]	k	Amplitude c_k [μm]	Phase ϕ_k [rad]
1	31.89	0.6021	1	43.38	5.2360
2	2.75	0.0349	2	4.05	0.0873
3	0.50	1.4312	3	0.35	1.1170
4	0.20	1.3963	4	0.25	0.2443
SUPPORT ROLLERS					
Drive Side			**Service Side**		
k	Amplitude c_k [μm]		k	Amplitude c_k [μm]	
	Front Roll	Rear Roll		Front Roll	Rear Roll
1	2.50	4.00	1	2.00	2.00
2	0.20	0.25	2	0.15	0.15
3	0.10	-	3	-	-

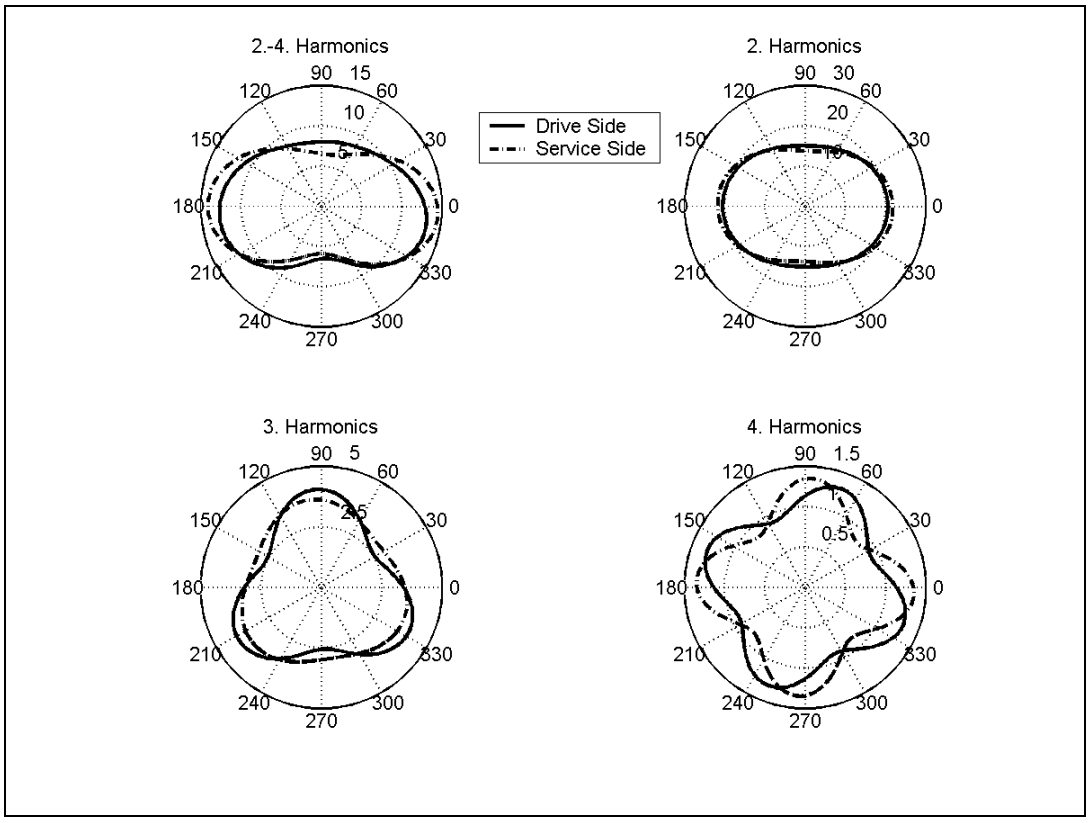

Figure 17. Graphical representation of the shafts waviness.

The waviness of the contacting bodies is modeled with splines in ADAMS. The roundness profiles of the shafts and support rollers are first calculated by using equation (3.10) in Matlab. The resulting roundness profiles as a function of rolls attitude angle α are imported to the ADAMS model. During simulation, these spline values are called by the Akima -spline fitting function. The usage of the splines is computationally very efficient; CPU times decreased about 50 % compared to direct calculation of the equation (3.10). The contact force function in equation (3.1) needs displacement variable and velocity variable. Examples of these are shown below.

```
Displacement_Variable=
1e3*DM(MAR,MAR_SFO)
+AKISPL(-YAW(MAR, MEA_cen)+pi/2-atan(77./92.),0,SPL_shaft, 0)
+AKISPL((MOD(115.0/125.0*-AZ(MAR, MEA_cen)+PI,2*PI)-PI),0,SPL_supp_roll, 0)

Velocity_Variable=
VR(MAR, MAR_SFO, MAR_SFO)
+1E-3*(AKISPL(-YAW(MAR, MEA_cen)+pi/2-atan(77./92.),0, SPL_shaft, 1)+
AKISPL((MOD(115.0/125.0*-AZ(MAR, MEA_cen)+PI,2*PI)-PI),0, SPL_supp_roll, 1))*
(-WZ(MAR, MEA_cen, MEA_cen))
```

Functions DM and VR are used to measure distance and velocity between the roll and support roller. Two splines are called in the displacement variable; the first spline is waviness of the shaft and the second is waviness of the support roller. Rolls attitude angle is measured with the YAW-function and given as an input to the spline function. Difference in diameters between shaft and support roller is taken into account. Unit of the displacement variable is intentionally selected to be μm, because the first and the second derivative of the power equation $F = k\delta^e$ is almost infinite, when $\delta \approx 0$. An average contact force in this case is 2500 N, which results in 5 μm penetration (see Figure 16). Thus the usage of micrometers is numerically more stable than the usage of millimeters. The waviness must be compensated from the velocity variable, because penetration velocity is required in equation (3.1). The spline fitting function AKISPL in the velocity variable returns the first derivative of the waviness with respect to rolls attitude angle. This must be multiplied by rolls angular velocity to obtain the line-of-sight velocity caused by waviness.

4 ASSEMBLED MODEL AND OPTIMIZATION

The model of the roller test rig is assembled by importing the flexible bodies described in chapter 2 and by defining rigid bodies as well as forces and constraints, which connect parts. The driving torque of the electric motor is not modeled. Instead of that a motion constraint is defined to drive the roll at the desired speed. The assembled model has following properties:

```
 113 Gruebler Count (approximate degrees of freedom)
   9 Moving Parts (not including ground)
   5 Flexible_Bodys
  17 Fixed Joints
   2 Inplane Primitive_Joints
   2 Orientation Primitive_Joints
   1 Motions

 113 Degrees of Freedom for .Roller
```

In ADAMS, modal damping ratios are used to describe internal damping of the flexible bodies. The modal damping ratios are defined in the DMPSUB subroutine as a function of modes frequency. However, these damping ratios are unknown, except the modal damping of the six lowest modes of the roll (see Table 5). Furthermore, the stiffness and damping coefficients of spring-damper forces are also unknown.

An experimental modal analysis was done also to the whole roller test rig [6]. Frequencies and damping ratios of 13 modes were measured (Table 11). In order to have a good agreement between the roller test rig and the simulation model, the modal parameters should be quite equivalent. ADAMS/Linear module calculates the same modal parameters from the full ADAMS model as resulted from measurement. The result set includes the natural frequencies, damping ratios and mode shapes. The theory of the linearization technique used in ADAMS/Linear is described in reference [11].

Table 11. Results of experimental modal analysis of the roll test rig [6].

N	Freq.	ζ %	comments	N	Freq.	ζ %	comments
1	29.83	0.608		2	32.16	1.06	
3	65.34	1.33		4	77.10	1.86	1)
5	87.36	3.01	1)	6	111.59	1.59	
7	137.62	1.99	2)	8	142.35	1.70	2)
9	159.56	1.42		10	179.04	2.10	
11	206.62	2.03		12	267.00	1.54	
13	282.78	1.12					
1) Modes are almost identical. However, two modes exists. 2) Modes are almost identical. Might be only one mode.							

It must be noted that not all modes are found in simulation model; modes 4 and 5 are only one mode in the model as well as modes 7 and 8. Average values of these modes are used in the optimization. Mode 9 does not exist in the simulation model, which leaves only 10 similar modes to optimize.

4.1 Optimization of modal parameters

To find the unknown parameters of the model, a Differential Evolution (DE) -algorithm is used. Differential Evolution is a quite recently developed optimization algorithm for stochastic non-linear optimization [12, 13]. The DE algorithm can be categorized into a class of evolutionary optimization algorithms. The functioning of DE is illustrated by simple example in Appendix I.

The optimization is performed by using the *Optimize* –program, which is developed in the Laboratory of Steel Structures in Lappeenranta University of Technology.

The optimization problem in this case can be summarized as follows: Find the optimum vector $X=(x_1,\ldots,x_n)$ of input parameters such that error Y between the modal parameters in the simulation model and measurement is minimal. The simulation model can be considered as a "black box" that receives the input vector X and returns an output Y. The main reasons for selecting the DE algorithm are:

- The target function is non-linear
- The number of input parameters is quite high
- No derivative information of target function is available, which prevents using gradient methods
- No analytical form of the target function is available
- Calculation of the target function is computationally costly, which prevents the usage of direct search.

The objective of optimization is to find input parameters, which results in similar damping ratios and frequencies of 10 modes. The selected target function Y for the optimization is

$$Y = \sum_{i=1}^{10} y_i, \qquad \textit{where}$$

$$y_i = \begin{cases} C_i \cdot \left| f_i - f_{mea\,i} \right|, & \left| 1 - \dfrac{c_i}{c_{mea\,i}} \right| \le 0.10 \\ C_i \cdot \left[10 \cdot \left| c_i - c_{mea\,i} \right| + \left| f_i - f_{mea\,i} \right| \right], & \left| 1 - \dfrac{c_i}{c_{mea\,i}} \right| > 0.10 \end{cases} \tag{4.1}$$

where y_i is the target function value for mode i, C_i is the weighting factor of the mode i (see Table 12), c_i is the modal damping ratio in the model and $c_{mea\,i}$ is the measured damping ratio, f_i and $f_{mea\,i}$ are model and measured frequencies, respectively. Error estimate for the measured damping is ± 10% and because of that the error in damping is neglected if it is less than 10 %. Because absolute error is used the error in damping is multiplied by 10 in order to increase its significance.

Selection of optimization design variables i.e. input parameters is not a trivial task. Design variables should have a significant effect to the target function. Furthermore they should be unambiguous, not like spring coefficient in serial connection, where the combined spring constant is achieved with infinite number of solutions. The selected design variables (Figure 18) are stiffness and damping coefficients of the spring-damper forces and modal damping ratios of the flexible parts. Modal damping ratios are defined according modes frequency. The modes whose frequency is higher than shown in Figure 18 are critically damped i.e. damping ratio is 100 %.

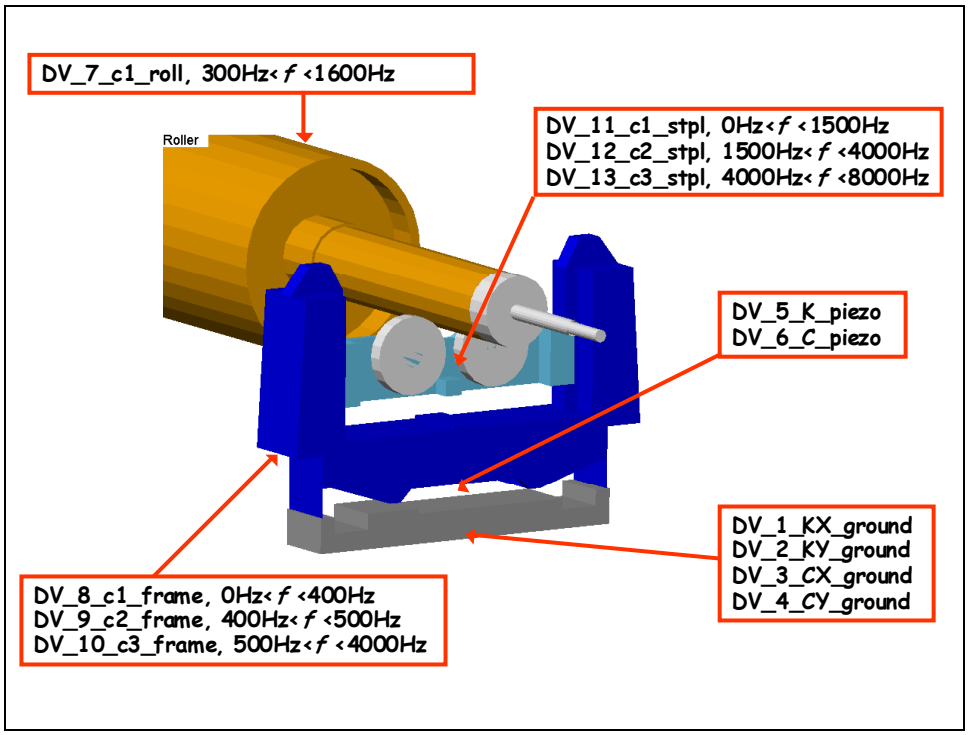

Figure 18. Design variables.

The optimization procedure works as follows:

1. Optimize –program calculates parameters for one individual
2. ADAMS reads in input parameters
3. Static Equilibrium analysis
4. Calculation of linear modes
5. Find frequencies and damping ratios and calculate target values y_i
6. Calculate final target function value Y and write it to a file *end.txt*
7. Optimize –program reads the result from *end.txt* and calculates parameters for the next individual

The optimization was run with the following parameters for 248 generations:

- Population size 20
- Mutation probability 0.98
- Differential factor 0.60.

The optimization results are shown in Table 12. Improvement in target function is more than 70 % and 9 of 10 damping ratios are within 10 % error limit. Lowest 6 frequencies agree very well. The results are presented graphically in Figures 19 and 20.

Table 12. Optimization results

Mode	Measured		Simulated								Weight. factor	Target function (absolute error)	
			Before Optimization				After Optimization						
	Damp. %	Freq. [Hz]	Damp. %	Error %	Freq. [Hz]	Error %	Damp. %	Error %	Freq. [Hz]	Error %	C	Before	After
1 (h)	0.608	29.83	0.344	43.4%	29.43	1.4%	0.580	4.6%	29.83	0.0%	10	30.432	0.021
2 (v)	1.060	32.16	0.286	73.0%	32.02	0.4%	1.137	-7.3%	32.08	0.2%	10	78.841	0.787
3 (h)	1.330	65.34	1.515	-13.9%	63.79	2.4%	1.388	-4.4%	65.68	-0.5%	5	16.977	1.681
4 (v)	1.680	82.23	1.406	16.3%	79.95	2.8%	1.847	-9.9%	81.09	1.4%	2	10.034	2.278
5 (h)	1.590	111.59	1.893	-19.1%	108.43	2.8%	1.748	-9.9%	110.93	0.6%	5	30.963	3.284
6 (v)	1.850	140.00	1.553	16.1%	138.82	0.8%	1.408	23.9%	140.15	-0.1%	2	8.300	9.143
7 (h)	2.100	179.04	1.927	8.2%	182.40	-1.9%	2.278	-8.5%	185.27	-3.5%	1.25	4.201	7.783
8 (h)	2.030	206.62	1.413	30.4%	224.18	-8.5%	1.884	7.2%	226.35	-9.6%	1.25	29.668	24.666
9 (v)	1.540	267.00	1.551	-0.7%	258.21	3.3%	1.694	-10.0%	259.24	2.9%	0.625	5.493	4.853
10 (h)	1.120	282.78	0.682	39.1%	307.97	-8.9%	1.011	9.7%	308.41	-9.1%	0.625	18.481	16.017
h = horizontal mode			Mean:	26.0%	Mean:	3.3%	Mean:	9.5%	Mean:	2.8%	Sum:	233.39	70.51
v = vertical mode											Improvement:		69.8%

The values of optimized parameters as well as their allowed range are shown in Table 13. The optimized values are quite reasonable, it was expected that modal damping ratios for high frequency modes are quite high.

Table 13. Optimized parameters.

Parameter	Range		Initial value	Optimal Value	Units
	min	max			
DV_1_KX_ground	100.00	2500.00	700.00	108.67	MN/m
DV_2_KY_ground	100.00	2500.00	700.00	302.74	MN/m
DV_3_CX_ground	1.00	100000.00	1000.00	8873.62	Ns/mm
DV_4_CY_ground	1.00	100000.00	1000.00	2238.97	Ns/mm
DV_5_K_piezo	60.00	80.00	70.00	75.69	MN/m
DV_6_C_piezo	1.00	100.00	5.00	9.32	Ns/mm
DV_7_c1_roll	0.01	10.00	0.50	0.72	%
DV_8_c1_frame	0.05	20.00	0.50	10.61	%
DV_9_c2_frame	0.05	20.00	0.50	6.61	%
DV_10_c3_frame	0.05	20.00	0.50	20.00	%
DV_11_c1_stpl	0.05	20.00	0.50	18.78	%
DV_12_c2_stpl	0.05	20.00	0.50	16.77	%
DV_13_c3_stpl	0.05	20.00	0.50	18.11	%

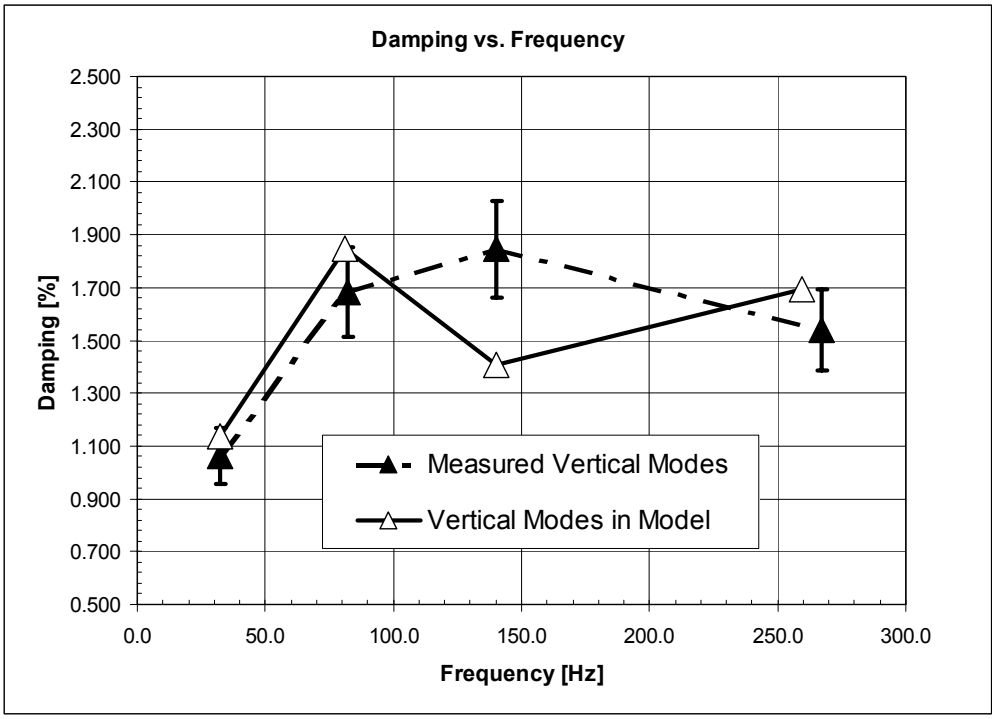

Figure 19. Damping and frequency of the vertical modes. Error estimate in damping is ± 10 %.

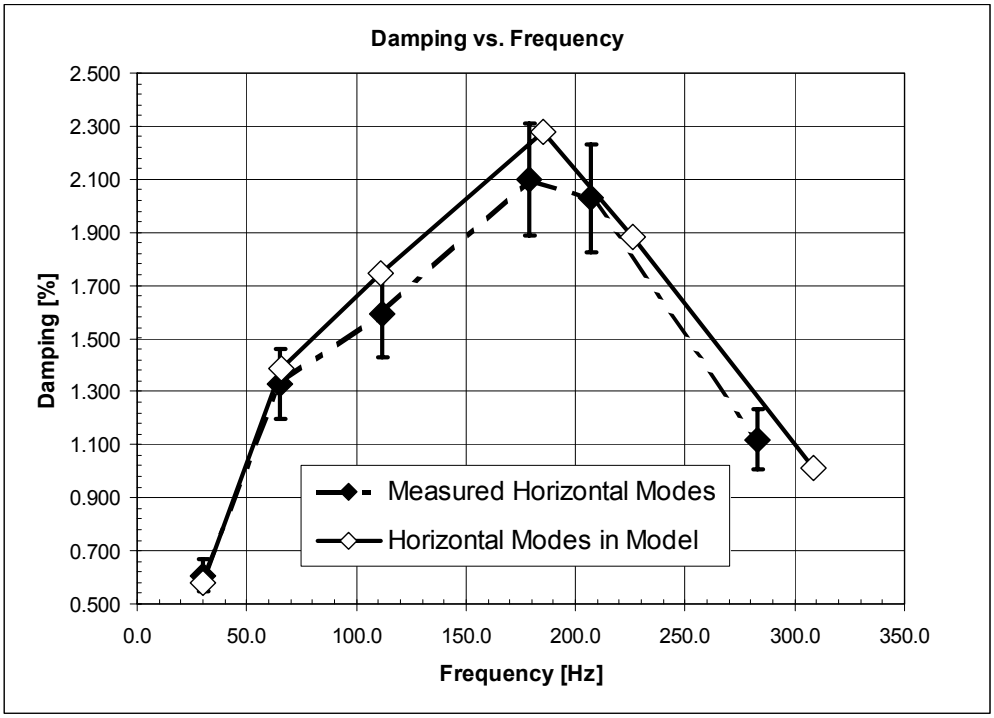

Figure 20. Damping and frequency of the horizontal modes. Error estimate in damping is ± 10 %.

5 VERIFICATION AND RESULTS

The simulation results are compared with those obtained by measuring the real structure. Horizontal and vertical throw is measured from three sections both from the simulation model and from the real structure. The results are compared by analysing the measured results of the throw with FFT in the frequency domain. The harmonic components of throw are used to generate data for the roll orbit plots in XY-plane.

5.1 Measurement in the roll test rig

The measuring equipment comprises a PC based data acquisition system, six laser sensors with amplifiers, connection panel and a guide bar in which the sensors have been installed. The throw of the roll is measured by using laser sensors whose function is based on the movement of the intensity maximum of the diffuse reflection of the laser beam with the detector. From the measured bend line, the throw and its harmonic components and resonance sections are analyzed. From the throw signal the sizes of the components, the mutual relations and phase angles and changes are perceived as a function of speed. The measurement points are shown in Table 14 and in Figure 21 [14].

Table 14. Measurement points in the roll test rig.

#	Measurement quantity	Sensor type	Unit
1	Drive side horizontal throw	Laser	μm
2	Drive side vertical throw	"	μm
3	Middle horizontal throw	"	μm
4	Middle vertical throw	"	μm
5	Service side horizontal throw	"	μm
6	Service side vertical throw	"	μm
7	Drive side pedestal acceleration	Acceleration	m/s^2
8	Service side pedestal acceleration	"	m/s^2
p	Pulse sensor (1/r and 1/1024r)	Pulse sensor	-

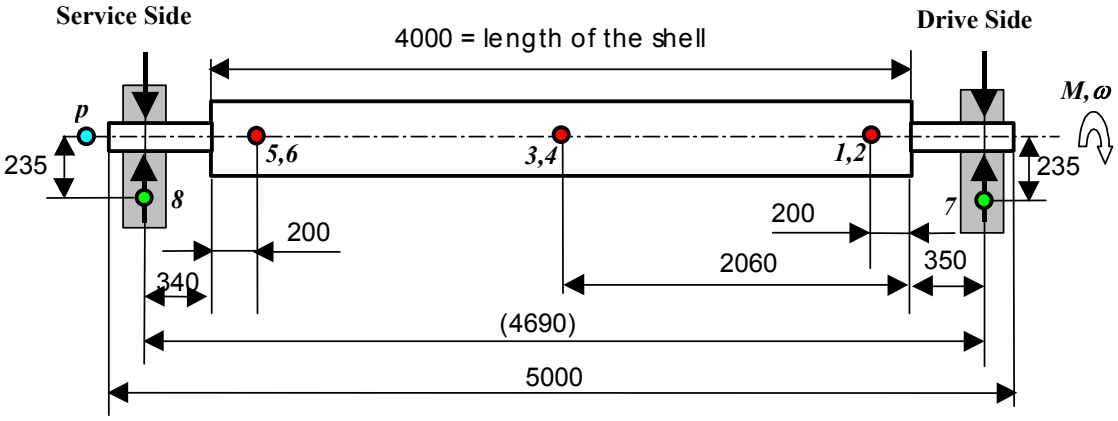

Figure 21. Measurement points of the roll.

5.2 Measurement in the simulation model

Throw is measured from the simulation model at the same locations than from the real roll. One of the disadvantages with flexible bodies in ADAMS is that measurements can be defined only on the nodal points. That is why the throw is measured differently than in reality. A measurement marker is defined on the top surface of the roll (Figure 22). Horizontal throw is measured with the following function:

```
THROW_X=1e3*(DX(MAR_MEA, MAR_ground, MAR_ground)+
        R_roll*(sin(YAW(MAR_MEA, MAR_ground))))
```

Correspondingly, the vertical throw is measured with the function:

```
THROW_Y=1e3*(DY(MAR_MEA, MAR_ground, MAR_ground)-
        R_roll*(cos(YAW(MAR_MEA, MAR_ground))))
```

Displacement is measured between the roll marker **MAR_MEA** and the ground marker **MAR_ground**. Displacement caused by roll rotation is compensated with trigonometric functions. The parameter **R_roll** is the outer radius of the roll. The YAW-function is used to measure roll rotation angle α. This measurement method causes errors if the radius of the roll changes. However, the selected modes of the roll do not contain local shell vibration modes and thus changes in the roll radius are unlikely.

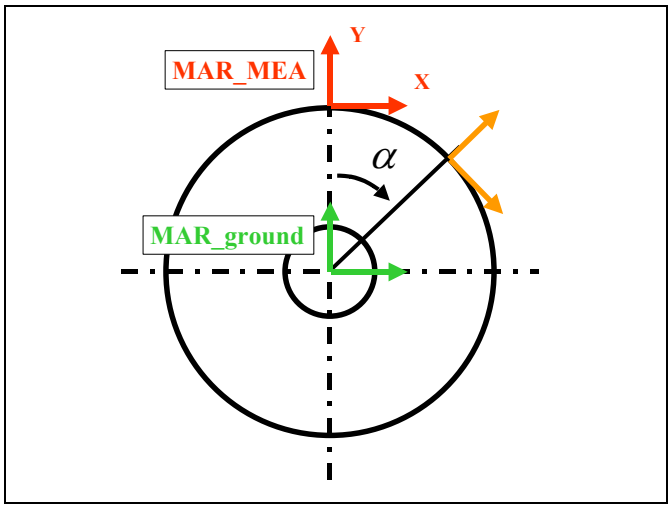

Figure 22. Measurement marker in the roll.

5.3 Data handling

The following signal processing procedures are applied both in the measured and simulated time domain data:

- Hanning –window averaging to time domain signal
- FFT (Fast Fourier Transform), 16384 points for measurement and 8192 for simulation results, both 8.192 s.
- Multiplication of the amplitude by 2 (Hanning correction)
- **Spectrum maps**
- Search of lowest 4 harmonics of the rotation speed
- Picket Fence correction for the frequency, amplitude and phase
- **Generation of roll orbits in xy-plane**

5.4 Simulation cases

The following simulation cases are analyzed:

CASE 1:
- Roll model with the parameters before optimization.

CASE 2:
- Roll model with the parameters after optimization.

CASE 3:
- The phase angles of the 2nd harmonics in shafts waviness is increased +220 degrees in both ends. This makes the phase angle of the minimum stiffness and the phase angle of waviness approximately same in the model and in the real roll. (See Figure 9 and Figure 17)
- Parameters after optimization.

CASE 4:
- Optimization is performed with slightly different target values; the modal damping of the first vertical bending mode (Mode 2) is decreased to 0.90 %. The optimization results are shown in Appendix III. This variation is almost within 10 % error of measured damping.
- Shaft waviness is as in *CASE 3*.

CASE 5:
- The shell thickness variation of the roll is two-fold (see Table 4). Stiffness variation is nearer to the real roll (see chapter 2.1.3).
- Other parameters are same as in *CASE 3*.

CASE 6:
- The amplitude of 2nd harmonics in shafts waviness is increased by +1 μm in both ends. This variation is within the error tolerance of the roundness measurement.
- Other parameters are same as in *CASE 3*.

CASE 7:
- Modal damping of the first vertical bending mode (Mode 2) is decreased to 0.90 %.
- The shell thickness variation of the roll is two-fold (see Table 4)
- The amplitude of 2nd harmonics in shafts waviness is increased by +1 μm in both ends
- Other parameters are same as in *CASE 3*.

5.5 Results

The simulation results are compared to measurements in this chapter. The measured spectrum map of the vertical throw in the middle of the roll is shown in Figure 23 and the corresponding horizontal spectrum map is shown in Figure 24. Equivalent spectrum maps of simulation cases 1 - 3 and 7 are shown in Figures 25-32. The spectrum maps in cases 4-6 are very similar than those of CASE 3 and thus they are not presented here.

All the modeled excitations can be seen from the simulated spectrum maps. Since the ratio between diameters of the shaft and support roller is 0.9, there are peaks at the frequencies 0.9, 1.8 and 2.7 times the rotation speed. The roll in the simulation model is not balanced as can be seen from the first harmonic component of the throw. However, the amount of imbalance does not affect to the higher harmonic components and thus imbalance is not considered in this study.

In all simulation as well as in measurements cases the amplitudes of horizontal 2^{nd} harmonics is greater than the vertical. This is caused by support of the roll and 2^{nd} order waviness of the shaft. In Figure 13 it is shown that the angle between the support rollers is 80°. When elliptical shaft rotates on this kind of support, the first contact is in peak and the second is in the valley of the waviness. This causes larger excitation in the horizontal direction than in the vertical direction. Furthermore, the support is more flexible in horizontal direction.

One-third critical resonance (3X-resonance) is not visible in the measured spectrum. However, from the simulated spectrum maps the resonance can be seen clearly. The simulated resonance amplitudes are quite large compared to half-critical resonance, because 3^{rd} order amplitudes of the waviness are less than 1 μm, whereas 2^{nd} order amplitudes are 2-4 μm. It is possible that the 3^{rd} order amplitude is zero in reality, because the error estimate in measurement is ± 1 μm. The reason for relatively high response in simulation results is probably caused by the type of support of the roll. When triangular shaft rotates on this kind of support, both contacts are near of peaks of the waviness. After 30° rotation of the roll both contacts are in valleys, respectively. This causes larger movement in vertical direction than equal sized 2^{nd} order waviness.

In the simulation CASE 1 the maximum amplitudes of 2^{nd} harmonics agree well with the measurement (see Table 15). However, there is two equal sized peaks in horizontal direction and the shape of the vertical resonance is wrong. The resonance peak is too sharp, which is due to small damping of the mode 2. This case was not expected to perform well, because parameters before optimization are used.

In the CASE 2 the horizontal amplitude of the 2^{nd} harmonics is very near of the measured one, but the frequencies do not agree. Horizontal half-critical resonance can be seen as a disturbance in the vertical spectrum map. Vertical maximum amplitude is smaller than the measured one. Spectrum map CASE 3 is similar to the CASE 2, but the amplitude of the vertical 2^{nd} harmonics is increased.

Spectrum map of the vertical throw in CASE 7 (Figure 31) is very similar to the measured one, except the 1^{st} harmonics which is increased due to increased imbalance. Shape and amplitude of the 2^{nd} harmonics agree very well both in horizontal and vertical direction.

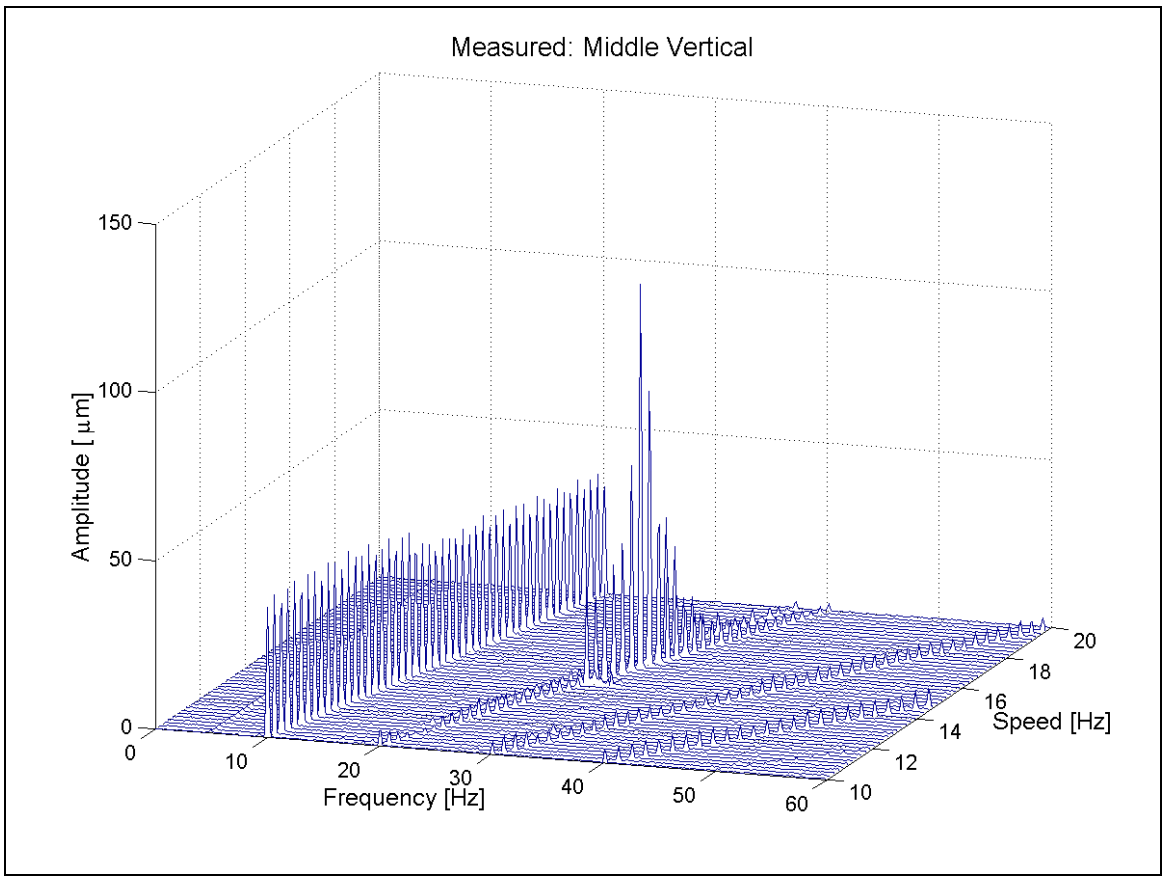

Figure 23. The measured (TP0) spectrum map of vertical throw in the middle of the roll.

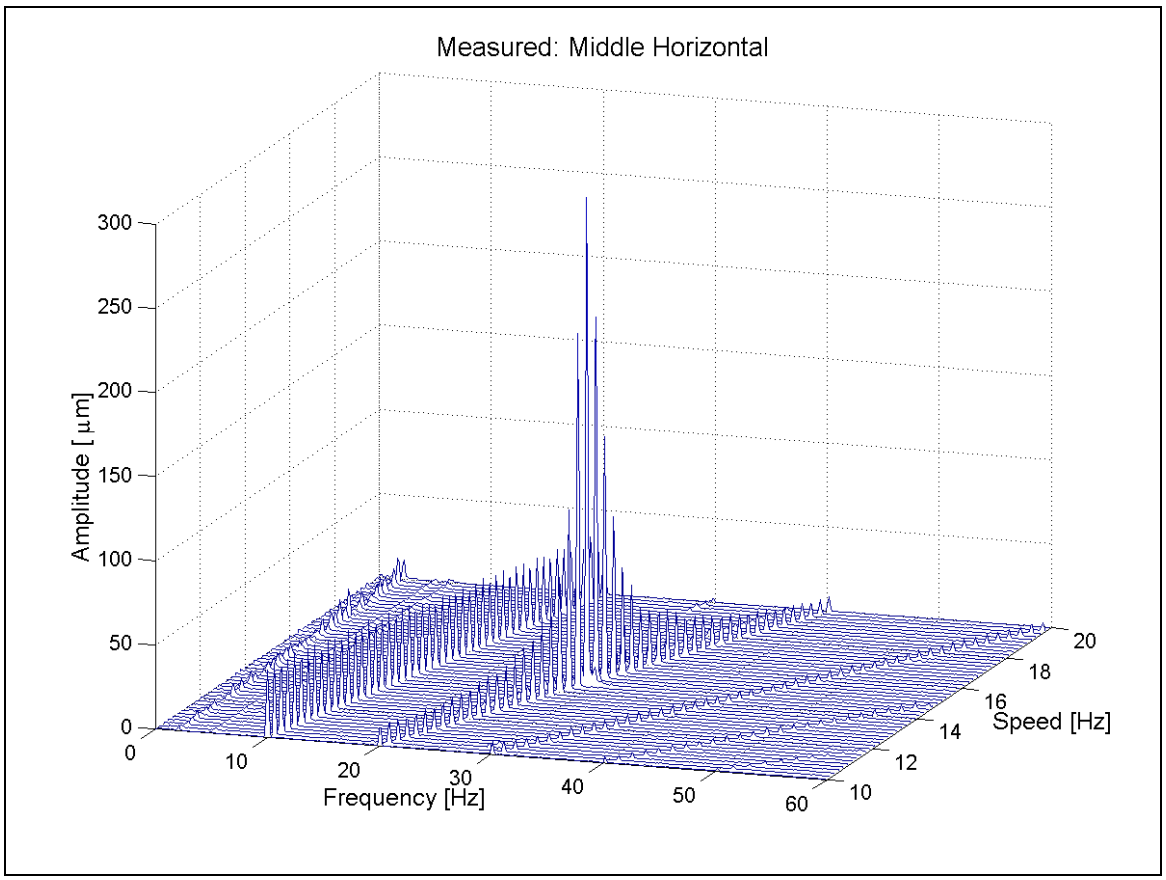

Figure 24. The measured (TP0) spectrum map of horizontal throw in the middle of the roll.

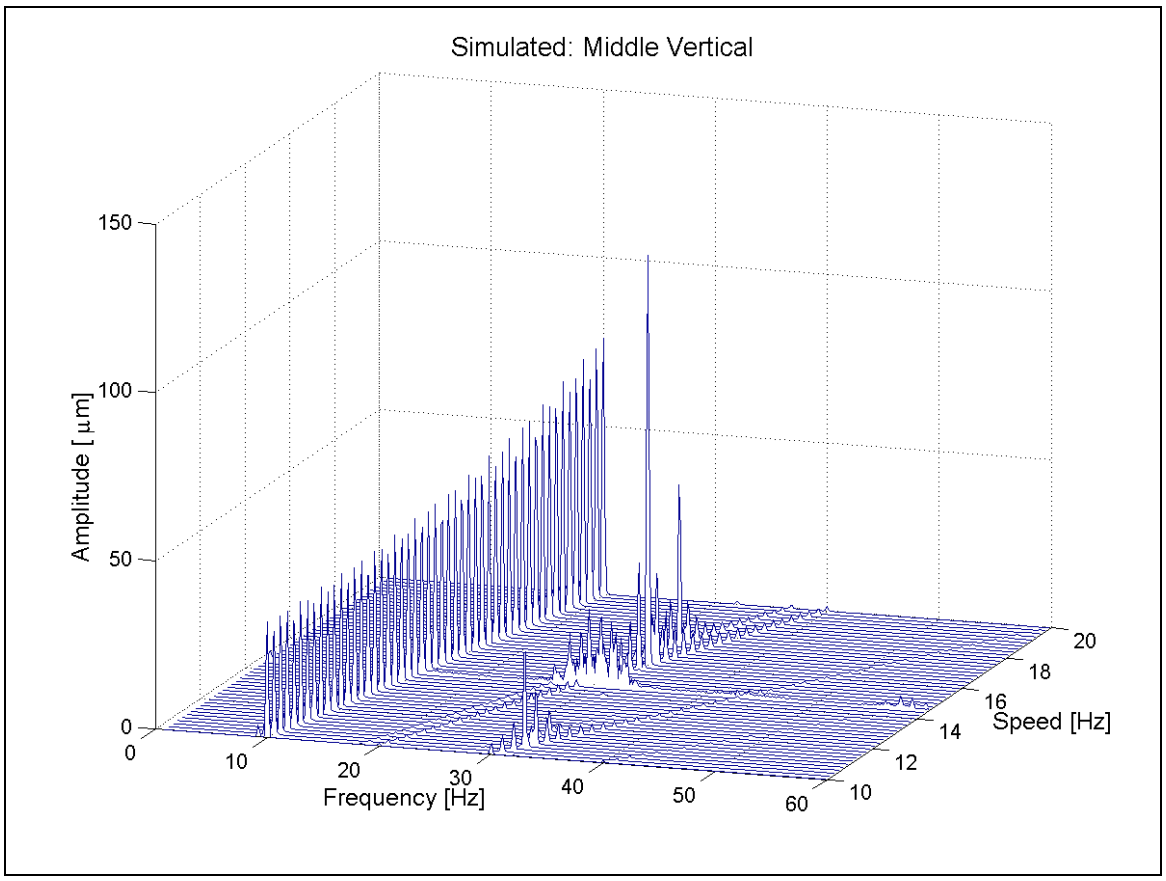

Figure 25. The simulated (CASE 1) spectrum map of vertical throw in the middle of the roll.

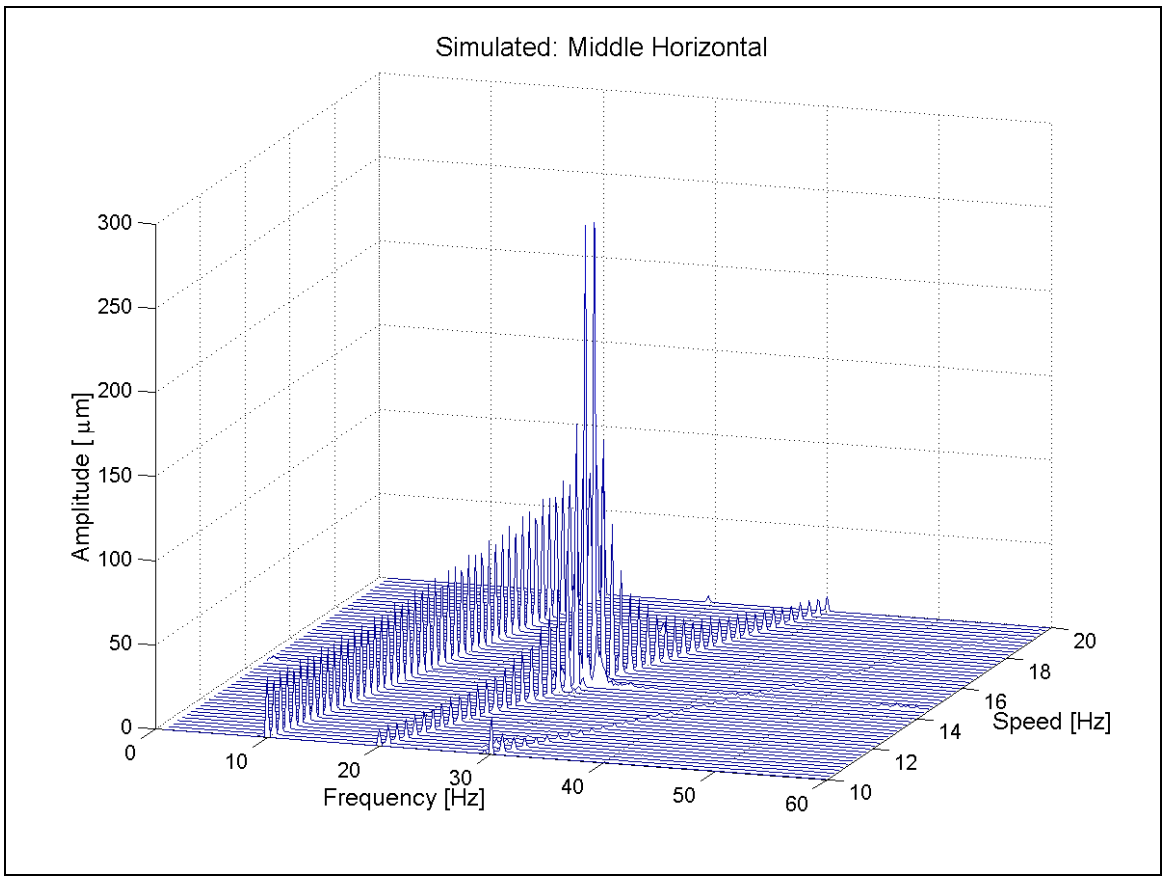

Figure 26. The simulated (CASE 1) spectrum map of horizontal throw in the middle of the roll.

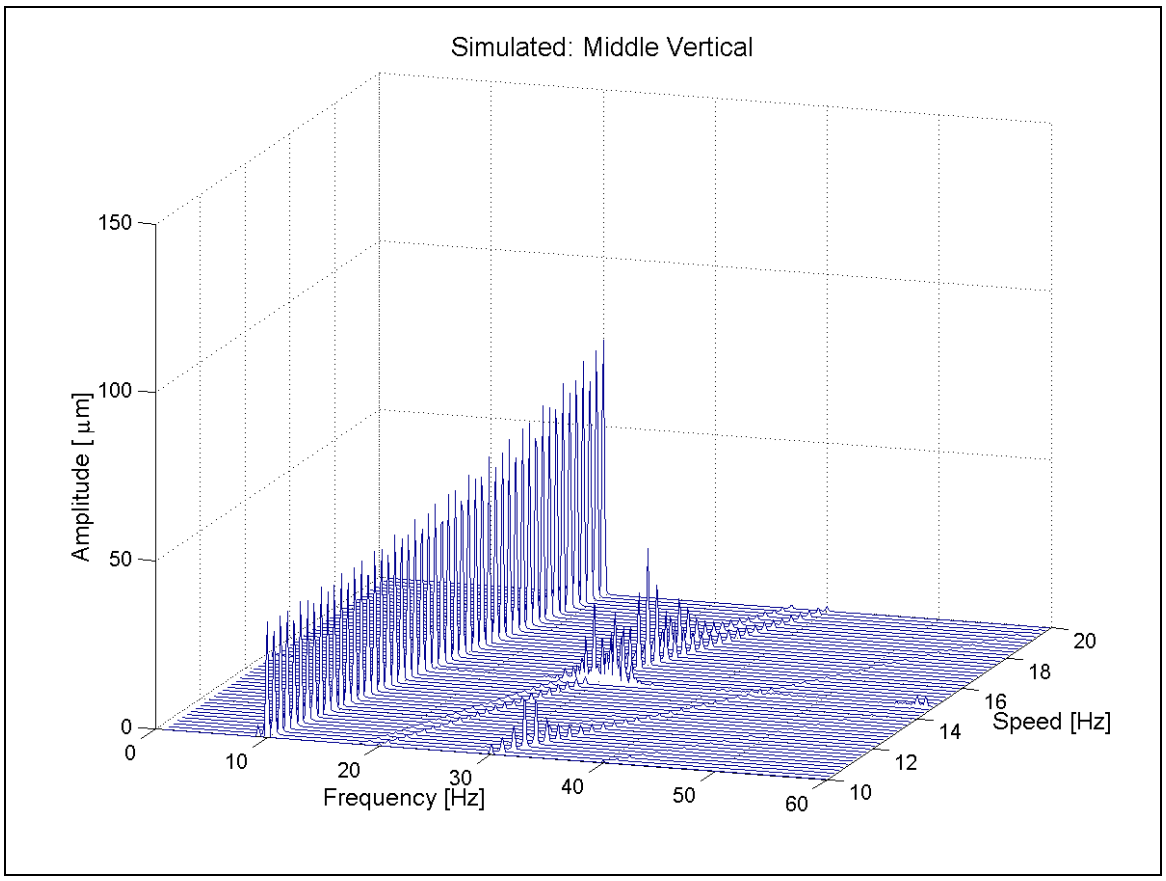

Figure 27. The simulated (CASE 2) spectrum map of vertical throw in the middle of the roll.

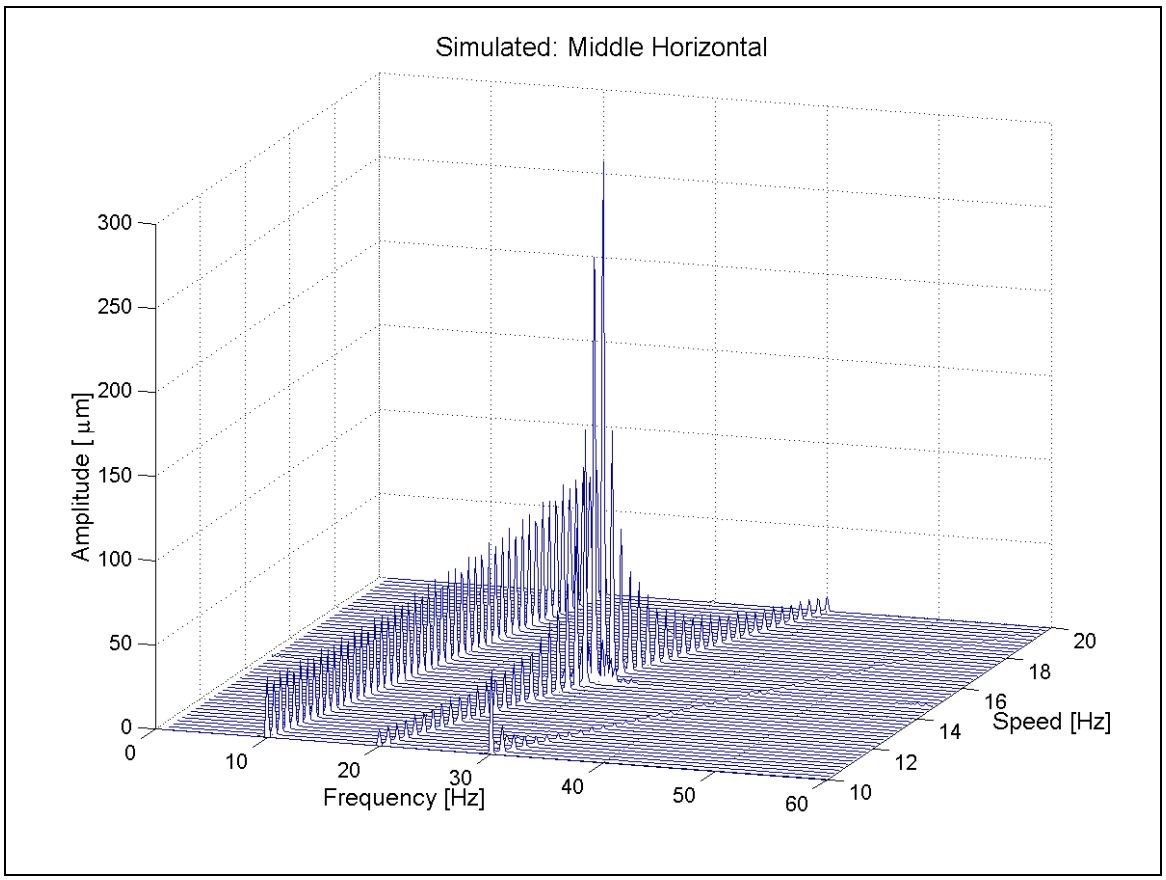

Figure 28. The simulated (CASE 2) spectrum map of horizontal throw in the middle of the roll.

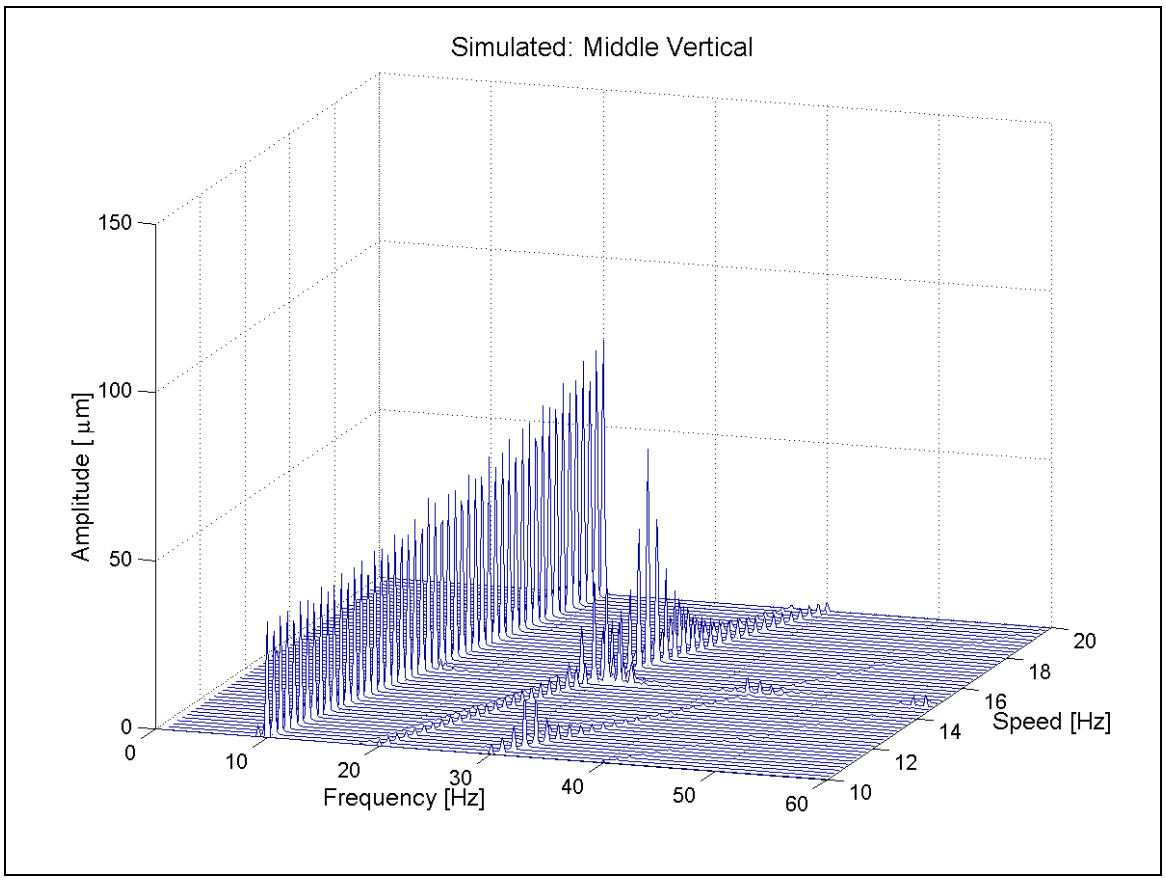

Figure 29. The simulated (CASE 3) spectrum map of vertical throw in the middle of the roll.

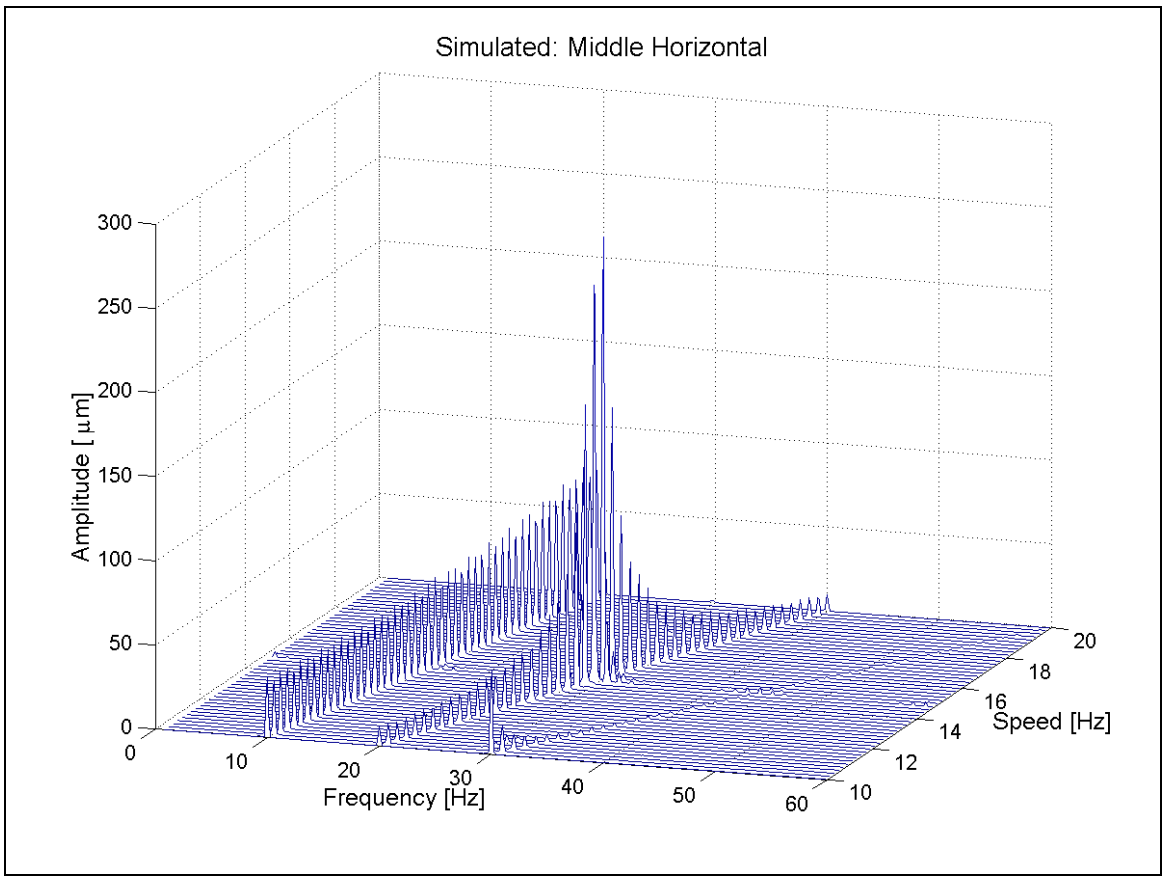

Figure 30. The simulated (CASE 3) spectrum map of horizontal throw in the middle of the roll.

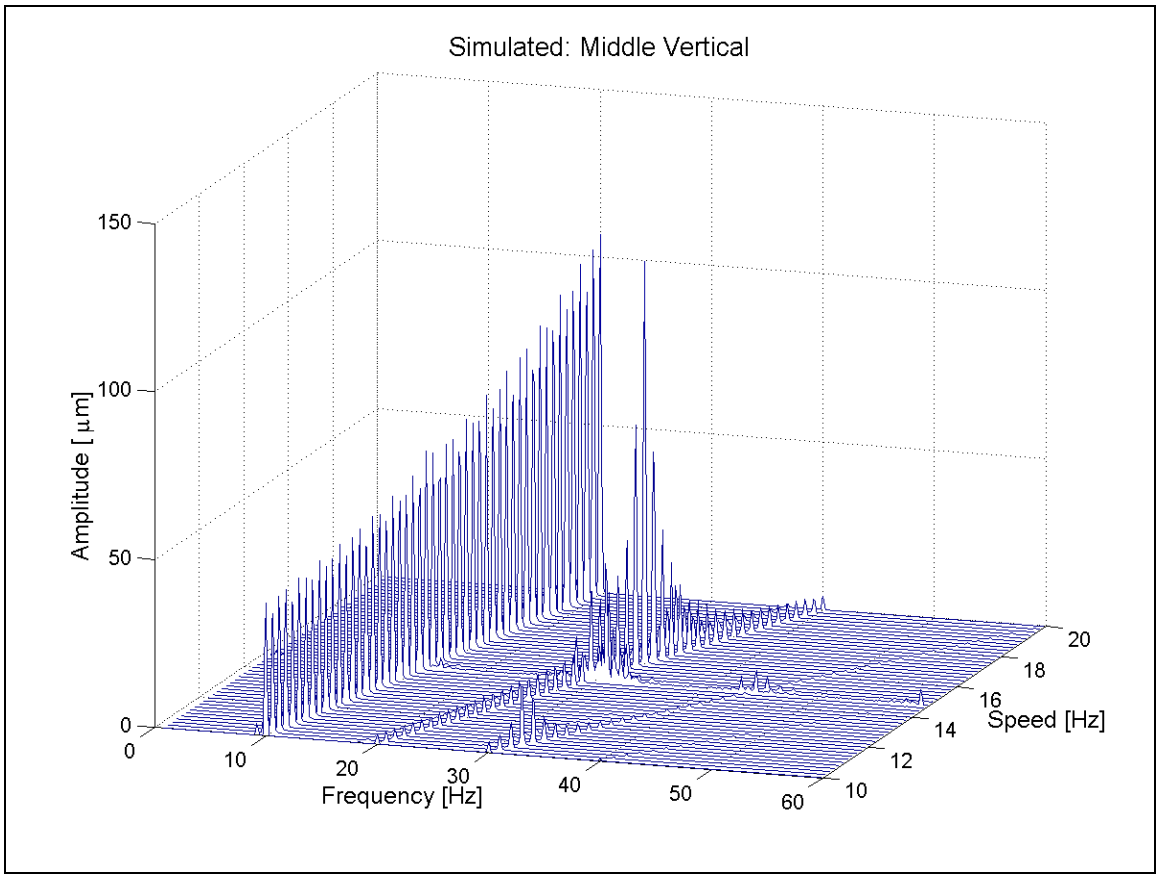

Figure 31. The simulated (CASE 7) spectrum map of vertical throw in the middle of the roll.

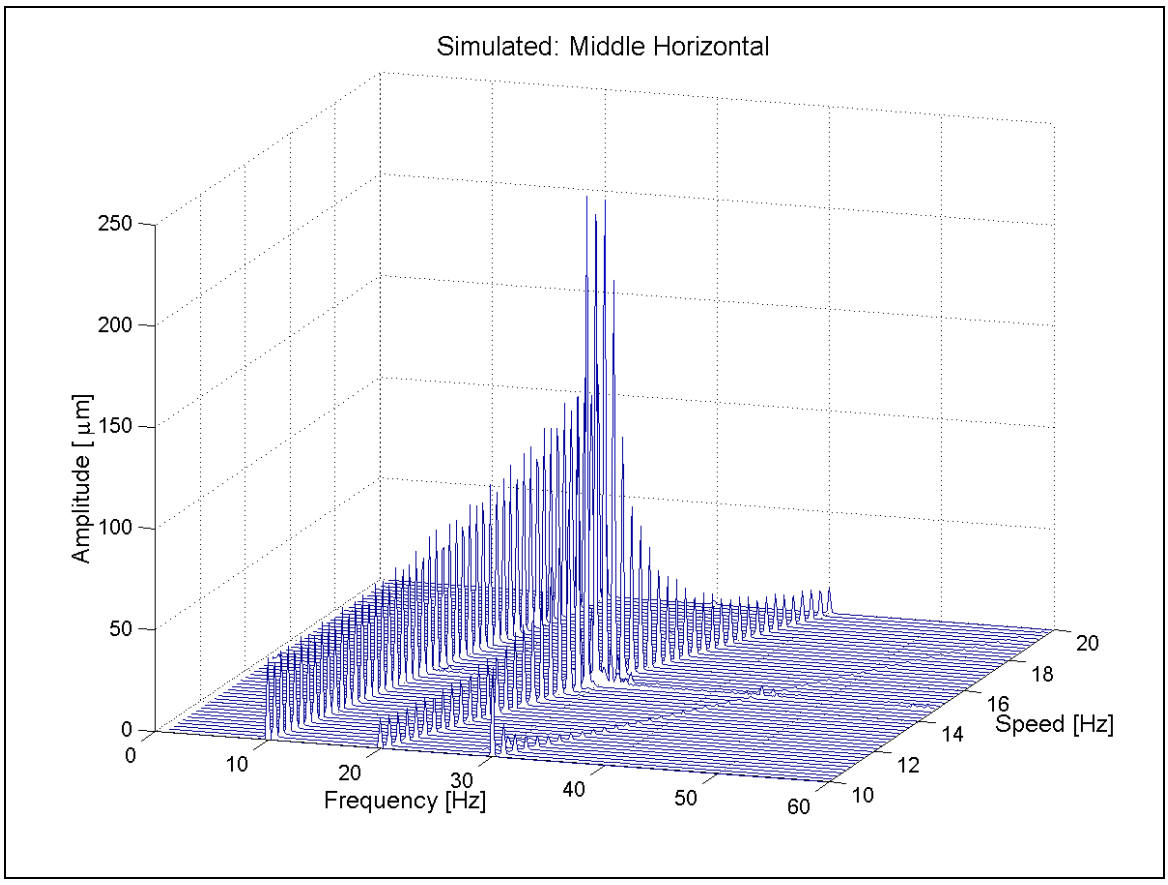

Figure 32. The simulated (CASE 7) spectrum map of horizontal throw in the middle of the roll.

Orbits of roll movement at different sections (Service Side, Middle, Drive Side) and at different speeds are shown in Figures 33 and 34. Data for orbit plots is generated from FFT results of the throw by taking into account 1st to 4th harmonic components of the throw. Rolls zero attitude angle is marked with a circle (o) and attitude angle increases to the direction of the blue line. There are small discrepancies between the phase angles of the harmonic components as well as amplitudes. This causes slightly different orbits in measurement and simulation, but the general movement of the roll is alike.

Amplitudes of 2nd harmonics in different simulation cases at the middle of the roll are shown in figures 35 and 36. The maximum amplitudes are listed in Table 15. The simulated horizontal amplitudes correspond very well to the measured ones. Variations in the simulation cases do not affect to the horizontal amplitude much. The measured maximum amplitude occurs at the rotation speed 14.6 Hz, which means that the first horizontal natural frequency is in reality 29.2 Hz, not 29.8 Hz as measured with modal analysis.

Vertical amplitudes vary in different simulation cases, which was expected. Variations to relative phase angle between stiffness variation of the roll and phase angle of the 2nd order waviness change the amplitudes significantly. According to the simulation results, the excitations caused by 2nd order waviness of the shaft and stiffness variation of the roll are in the same phase when the peaks of the 2nd order waviness are coincident with the minimum stiffness direction. In the CASE 2, these two excitations are acting against each other and in the CASE 3 they are acting in the same phase. Thus maximum amplitude of the vertical half critical resonance is increased by 30 μm from CASE 2 to CASE 3.

Maximum amplitudes in cases 4 to 6 are practically same. It seems that decrease in damping of the first vertical bending mode (CASE 4), increase in stiffness variation (CASE 5) and increase in 2nd order waviness (CASE 6) causes similar increase in response. Increase in maximum amplitude is about 15 μm in each case. In the CASE 7, all the above-mentioned variations are combined and the maximum amplitude is very near to the measured one.

It can be said that the simulation model can predict half critical responses accurately. Variations in different simulation cases are within error limit of the measured initial data. Especially the stiffness variation of the roll can be larger than in the simulation model.

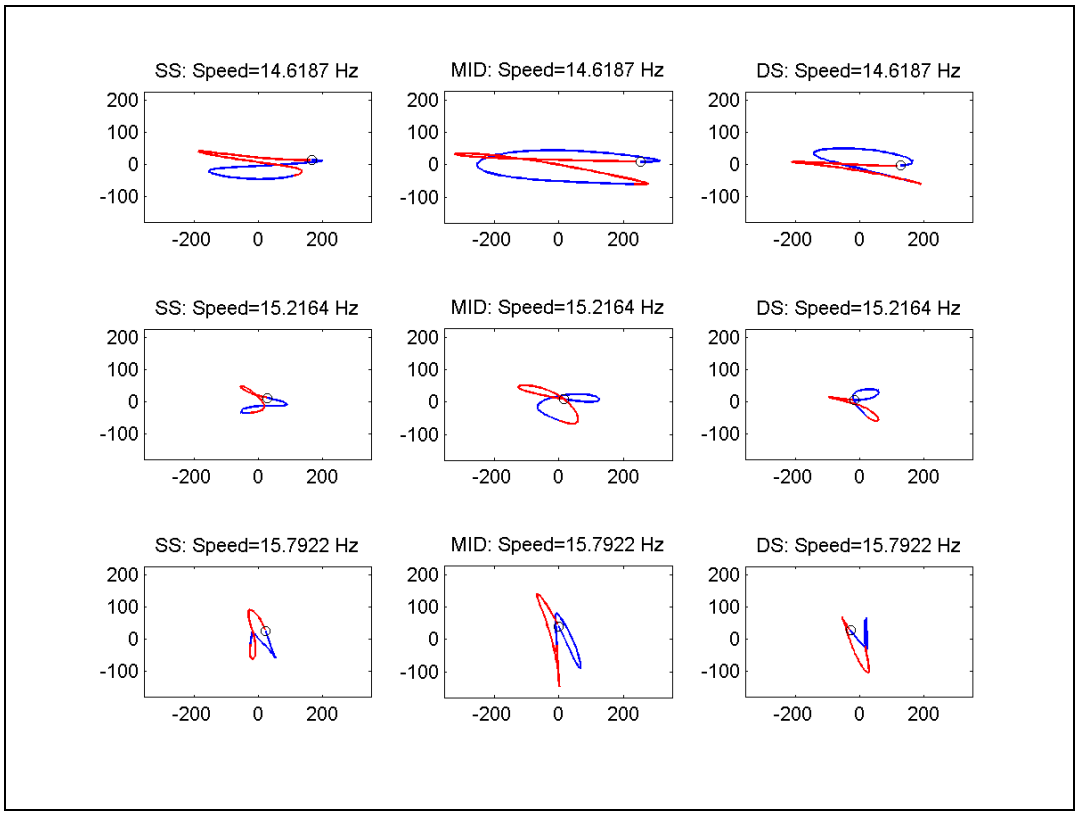

Figure 33. Measured (TP0) roll orbits at horizontal half critical speed (top row), between half critical speeds (middle row) and at vertical half critical speed (bottom row). SS=Service Side, MID=Middle, DS=Drive Side.

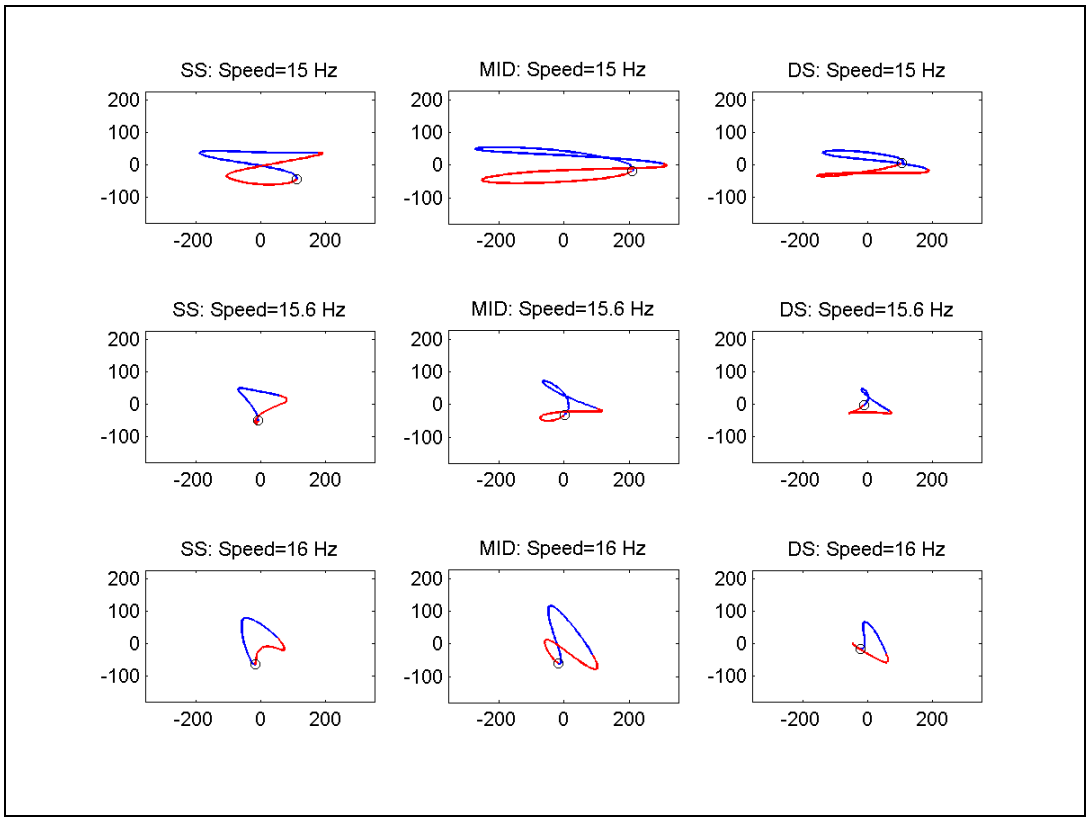

Figure 34. Simulated (CASE3) roll orbits at horizontal half critical speed (top row), between half critical speeds (middle row) and at vertical half critical speed (bottom row). SS=Service Side, MID=Middle, DS=Drive Side.

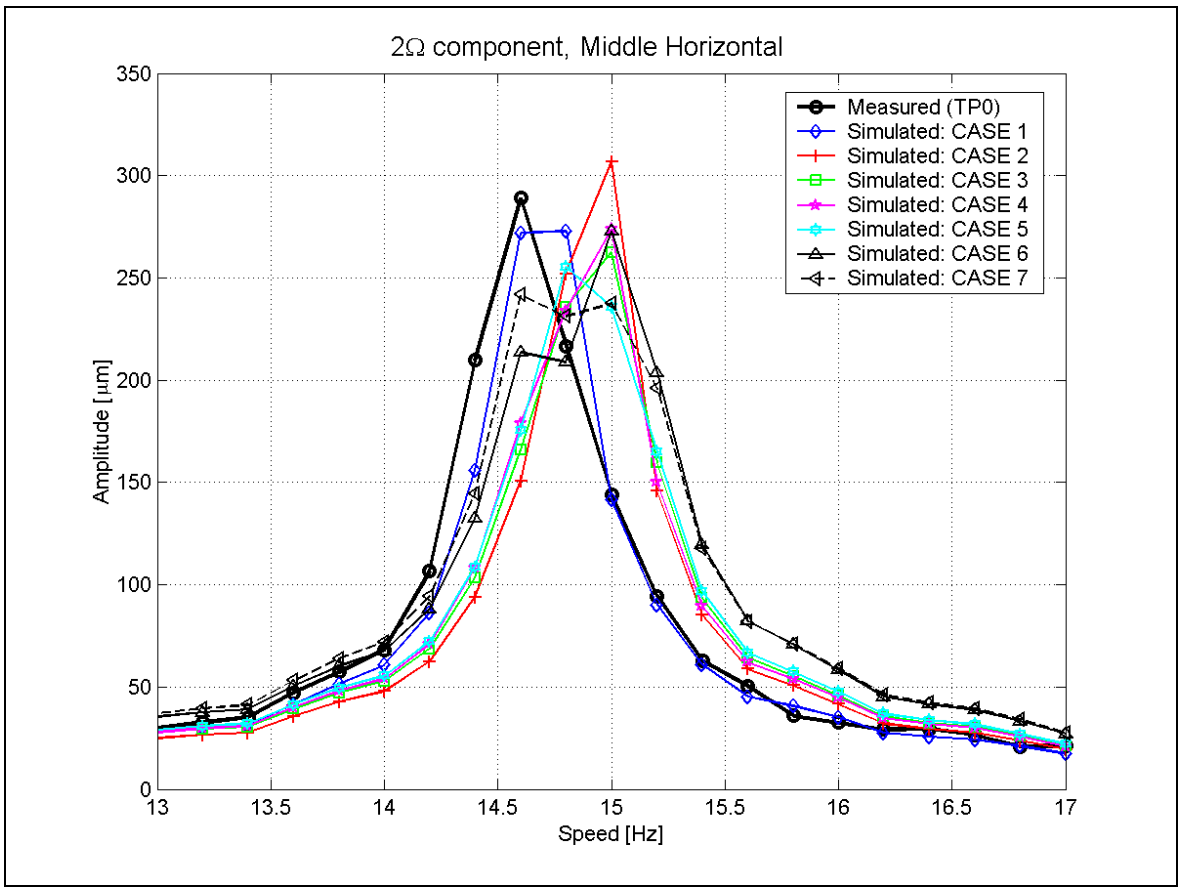

Figure 35. Amplitudes of the horizontal 2nd harmonics at middle.

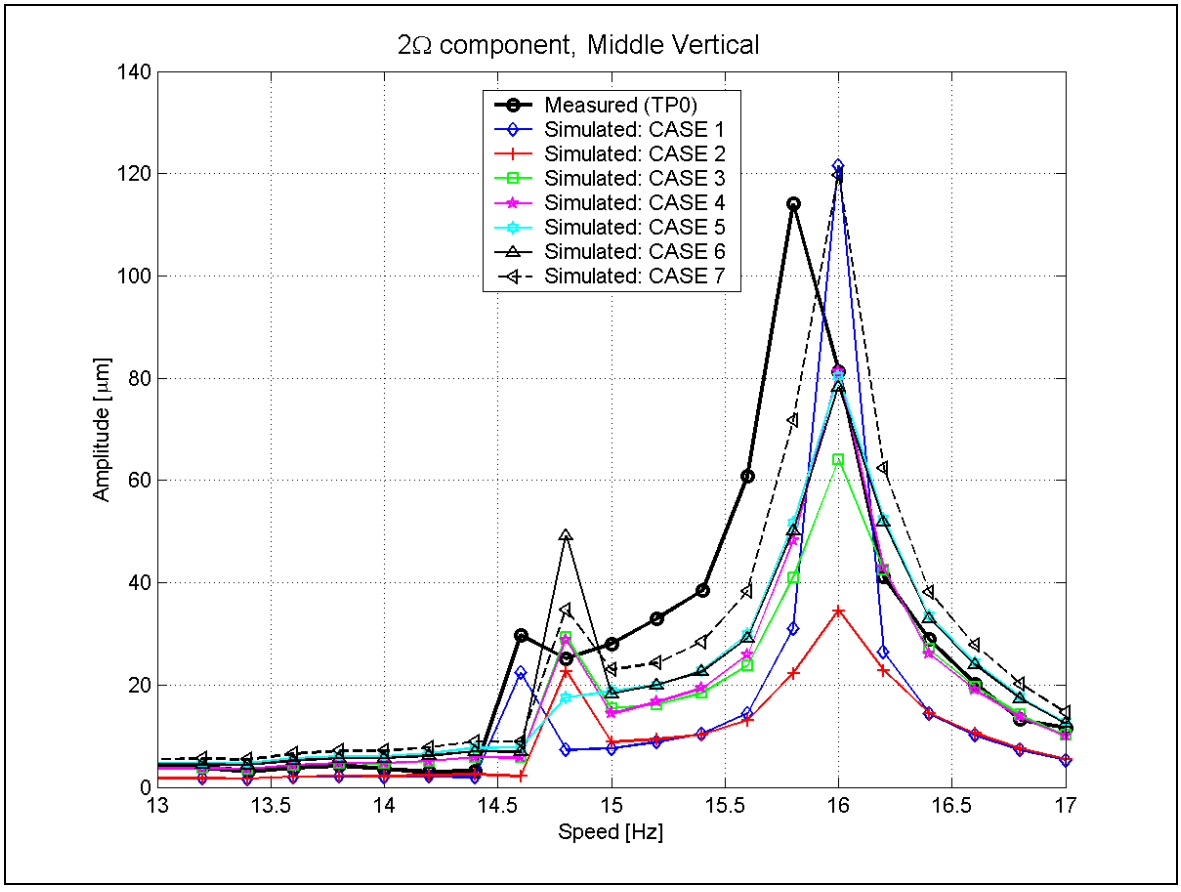

Figure 36. Amplitudes of the vertical 2nd harmonics at middle.

Table 15. Maximum amplitudes of 2nd harmonics.

Channel	**Measured** μm @ Hz	**CASE 1** μm @ Hz	**CASE 2** μm @ Hz	**CASE 3** μm @ Hz
Drive Side Horizontal	176 @ 14.6	158 @ 14.6	173 @ 15.0	147 @ 15.0
Drive Side Vertical	66 @ 15.8	62 @ 16.0	18 @ 16.0	33 @ 16.0
Middle Horizontal	289 @ 14.6	273 @ 14.8	307 @ 15.0	263 @ 15.0
Middle Vertical	114 @ 15.8	122 @ 16.0	35 @ 16.0	64 @ 16.0
Service Side Horizontal	167 @ 14.6	159 @ 14.6	171 @ 15.0	147 @ 15.0
Service Side Vertical	56 @ 15.8	62 @ 16.0	18 @ 16.0	33 @ 16.0
Channel	**CASE 4** μm @ Hz	**CASE 5** μm @ Hz	**CASE 6** μm @ Hz	**CASE 7** μm @ Hz
Drive Side Horizontal	154 @ 15.0	147 @ 14.8	154 @ 15.0	139 @ 14.6
Drive Side Vertical	41 @ 16.0	41 @ 16.0	40 @ 16.0	61 @ 16.0
Middle Horizontal	274 @ 15.0	255 @ 14.8	273 @ 15.0	242 @ 14.6
Middle Vertical	81 @ 16.0	80 @ 16.0	78 @ 16.0	120 @ 16.0
Service Side Horizontal	153 @ 15.0	144 @ 14.8	153 @ 15.0	141 @ 14.6
Service Side Vertical	42 @ 16.0	41 @ 16.0	40 @ 16.0	61 @ 16.0

6 ADDITIONAL SIMULATIONS

The results of various types of simulations are presented in this chapter. These simulations are not directly compared to measurements, since variations are mainly in modeling aspects. Mode selection of the flexible bodies is studied in CASE 8 and inertia modeling of the roll is studied in Cases 9 and 10. Vertical half critical resonance is caused by stiffness variation of the roll and 2nd order waviness of the shafts. These excitations cannot be excluded from the existing roll. That is why the effects of stiffness variation of the roll and waviness of the shafts are studied separately in cases 11-15.

6.1 Selection of the modes

Mode selection of the flexible parts is discussed in chapter 2. Mode selection in dynamic analysis is a very demanding task, and the set of selected modes affect to results greatly. To ensure the validity of the selected modes, a simulation with all modes in all flexible parts is performed. Model degrees-of-freedom are increased from 113 to 287, which means considerable increase in CPU-time. The simulation CASE 8 can be summarized as follows

CASE 8
- All modes in flexible parts are selected
- Otherwise same as CASE 3

Natural frequencies of the model are almost same, except for the first horizontal mode. Its frequency is decreased from 29.8 Hz to 28.9 Hz. Furthermore, more vibration modes is found from the model, which is explained by the increase in degrees-of-freedom. The frequency of the first horizontal mode corresponds well with the measured spectrum, but not with the experimental modal analysis. Change in frequency is probably due to increased flexibility of the pedestal parts.

Spectrums of the vertical throw at the middle of the roll in cases 3 and 8 are compared in Figure 37, where the absolute value of amplitude difference is presented. The only significant difference is the shift in the frequency of the first horizontal mode. First harmonic component is practically same in cases 3 and 8. According to this result, the selection of vibration modes is correct.

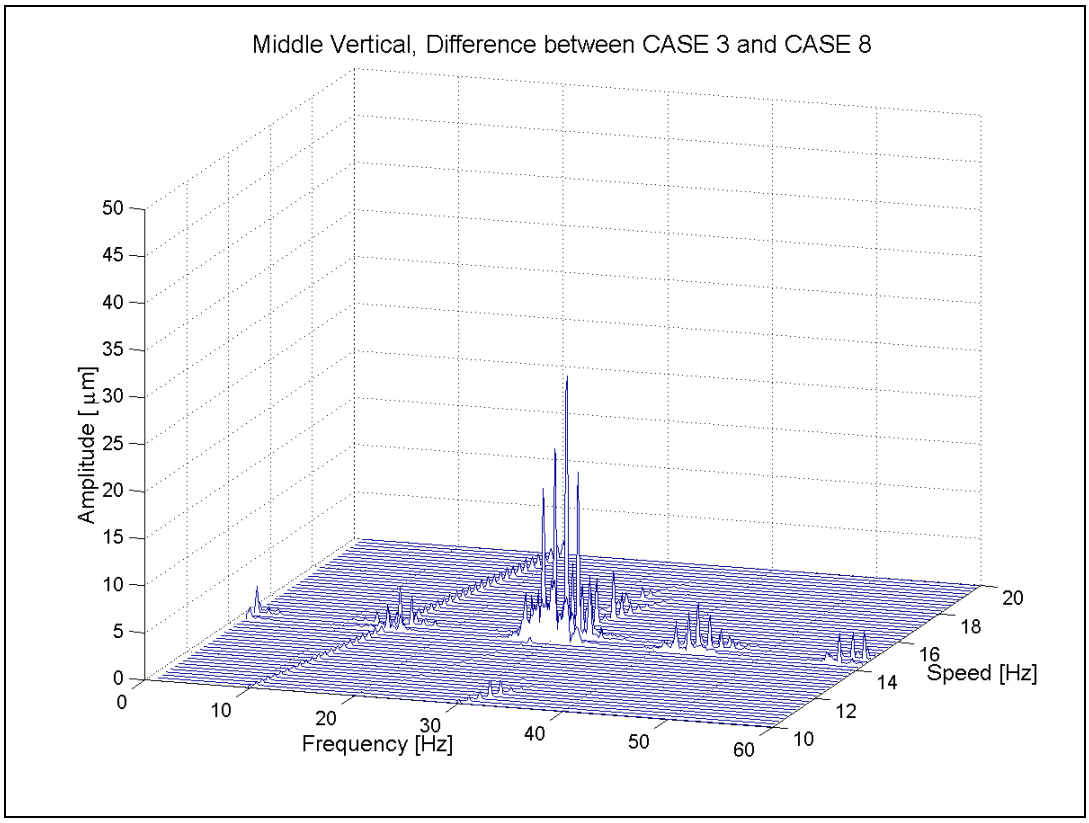

Figure 37. Absolute difference between vertical throw at middle in cases 3 and 8. The only significant discrepancy is the shift in the frequency of the first horizontal mode. Otherwise spectrums are identical.

6.2 Inertia modeling of the roll

The mass matrix of the flexible body is a highly non-linear function of the generalized coordinates of the body reference frame as well as deformation of the body. ADAMS computes the time varying mass matrix by using nine inertia invariants [4, 8]. The selection of invariants is shown in Figure 38. All the previous cases were run with all invariants in the roll enabled. However, invariants $\mathbf{I}^5$ and $\mathbf{I}^9$ are computationally most expensive, but their contribution to the results is sometimes negligible.

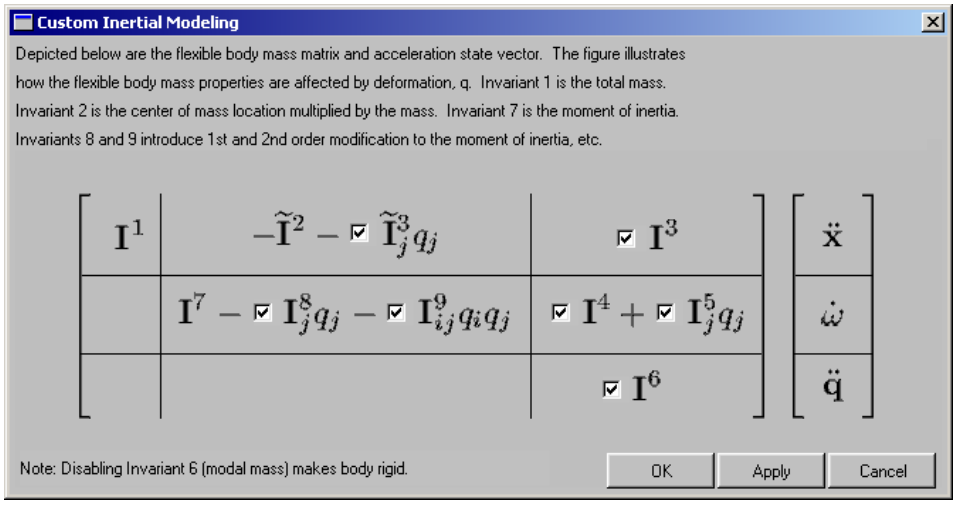

Figure 38. Selection of the inertia invariants in ADAMS.

Cases 9 and 10 can be summarized as follows:

CASE 9

- Same as CASE 3, but invariants $\mathbf{I}^5$ and $\mathbf{I}^9$ are disabled (Partial Coupling)

CASE 10

- Same as CASE 3, but invariant $\mathbf{I}^9$ is disabled (Custom Inertia modeling)

The spectrum map of the vertical throw in the CASE 9 is shown in Figure 39. This spectrum differs from the measured one as well as from the CASE 3 significantly. A very strong cross coupling between the vertical and the horizontal direction is visible. This phenomenon can be seen also from Figure 40, where roll orbits are shown. CASE 10 is run with inertia invariant 9 disabled, but invariant 5 enabled. The spectrum map of the vertical throw in the CASE 10 is shown in Figure 41. Spectrum corresponds very well with the CASE 3, which means that inertia invariant $\mathbf{I}^5$ is significant in the roll system modeling. Invariant $\mathbf{I}^5$ is a second-order correction of the rotation and deformation cross coupling and invariant $\mathbf{I}^9$ is a second-order correction to the inertia tensor of the flexible body.

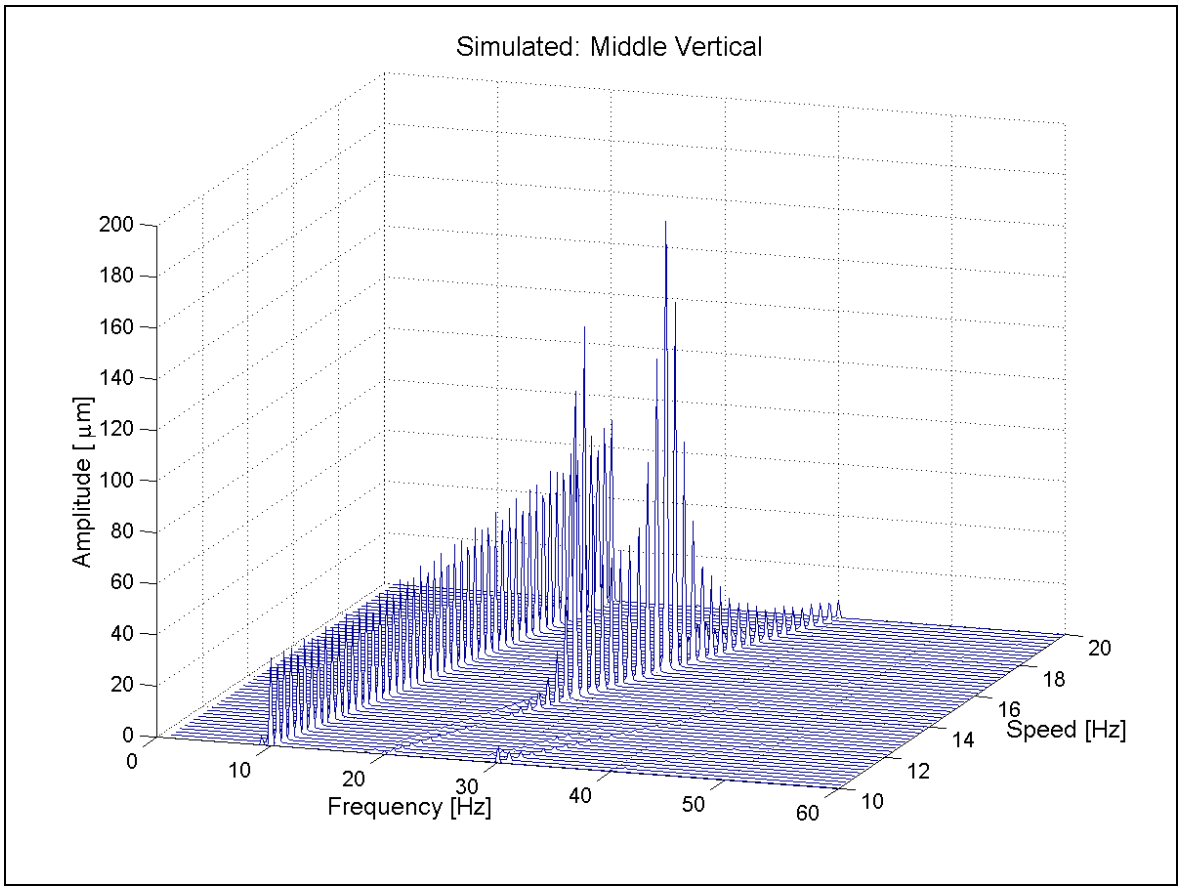

Figure 39. The simulated (CASE 9) spectrum map of vertical throw in the middle of the roll.

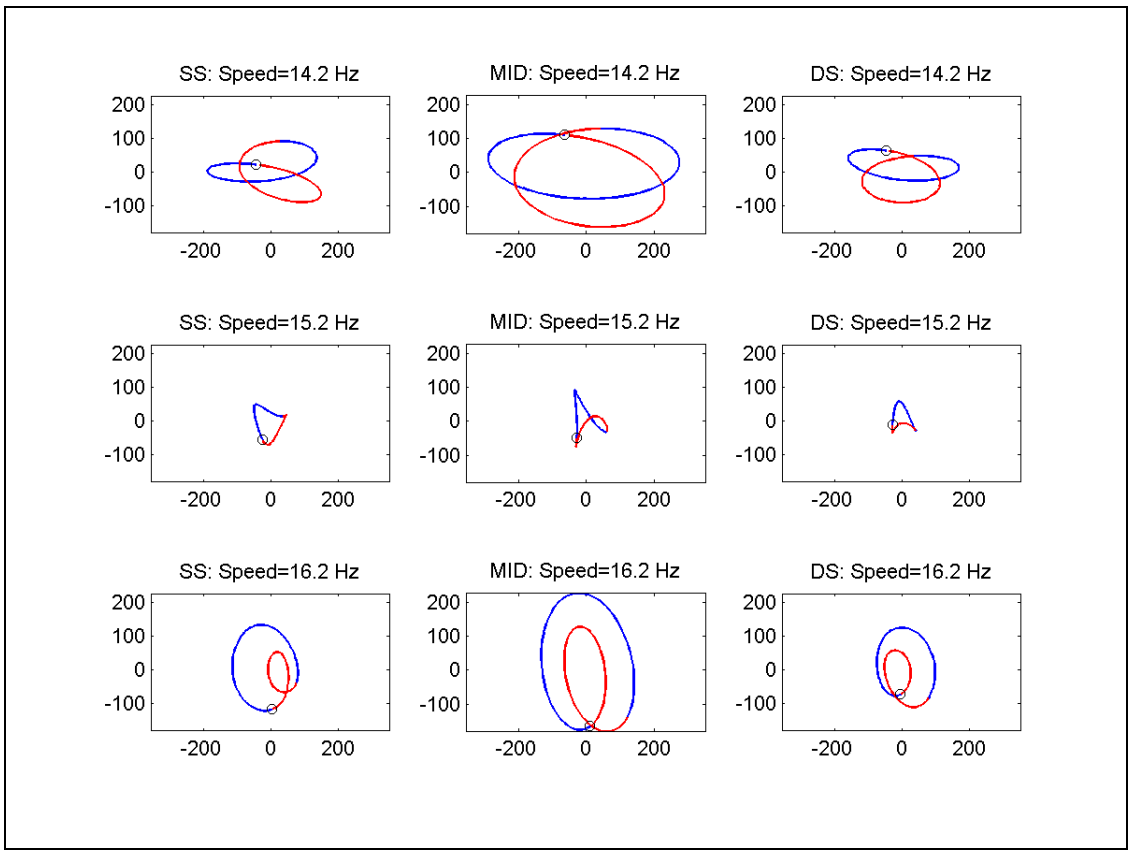

Figure 40. Simulated (CASE9) roll orbits at horizontal half critical speed (top row), between half critical speeds (middle row) and at vertical half critical speed (bottom row). SS=Service Side, MID=Middle, DS=Drive Side.

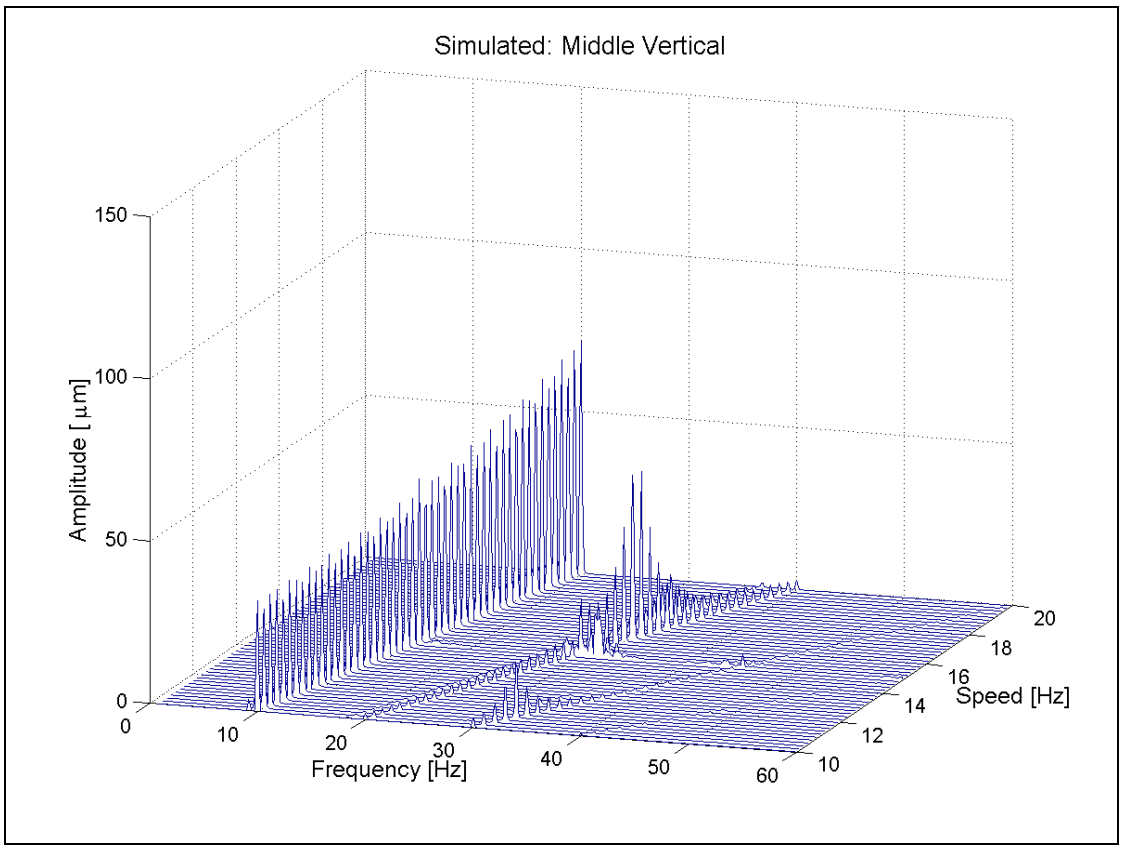

Figure 41. The simulated (CASE 10) spectrum map of vertical throw in the middle of the roll.

6.3 Effect of stiffness variation of the roll and waviness of the shaft

As mentioned before, the half critical resonance is caused by the stiffness variation of the roll and the 2nd order waviness of the shaft necks. The effect of these two reasons is studied in the cases 11-15, which are summarized below.

CASE 11
- Ideal roll (no shell thickness variation)
- Waviness of the shaft same as in the CASE 3

CASE 12
- Normal shell thickness variation
- Ideal shafts (no waviness)

CASE 13
- Shell thickness variation two-fold
- Ideal shafts (no waviness)

CASE 14
- Phase angles of the 2nd and 3rd harmonic components of the shaft waviness are opposite in the service and drive side. Phase angles are increased by +180 degrees at the service side (see Figure 46).
- The roll is ideal i.e. no shell thickness variation is modeled
- 1st harmonic component in shaft waviness is removed

CASE 15
- The amplitudes of the 2nd and 3rd order waviness is increased by +2 μm at both sides
- The roll is ideal i.e. no shell thickness variation is modeled
- 1st harmonic component in shaft waviness is removed

The spectrum map of the vertical throw in the CASE 11 is shown in Figure 42 and corresponding horizontal spectrum is shown in Figure 43. These spectrums are very similar than those of the CASE 3. It seems that stiffness variation has not significant effect to the half critical vibration response in this case. Spectrums of the vertical throw in the middle of the roll in cases 12 and 13 are shown in Figures 44 and 45. Second order response is small compared to the CASE 11.

Amplitudes of the second order harmonics are quite small in the CASE 14 (Figure 47), where the phase angles of the waviness are opposite. First order harmonics does not exist, small peaks are due to support roller waviness and their frequency is $0.9 \cdot \Omega$. Amplitudes of the 3rd harmonics are also negligible.

In the CASE 15 (Figure 49 and Figure 50), the amplitudes of the 3rd harmonics are increased greatly compared to the CASE 11. The amplitude of the vertical 3rd harmonics is almost equal as the amplitude of the 2nd harmonics.

Amplitudes of the horizontal 2nd harmonics at middle of the roll in cases 11-15 are shown in Figure 51 and corresponding vertical amplitudes are shown in Figure 52.

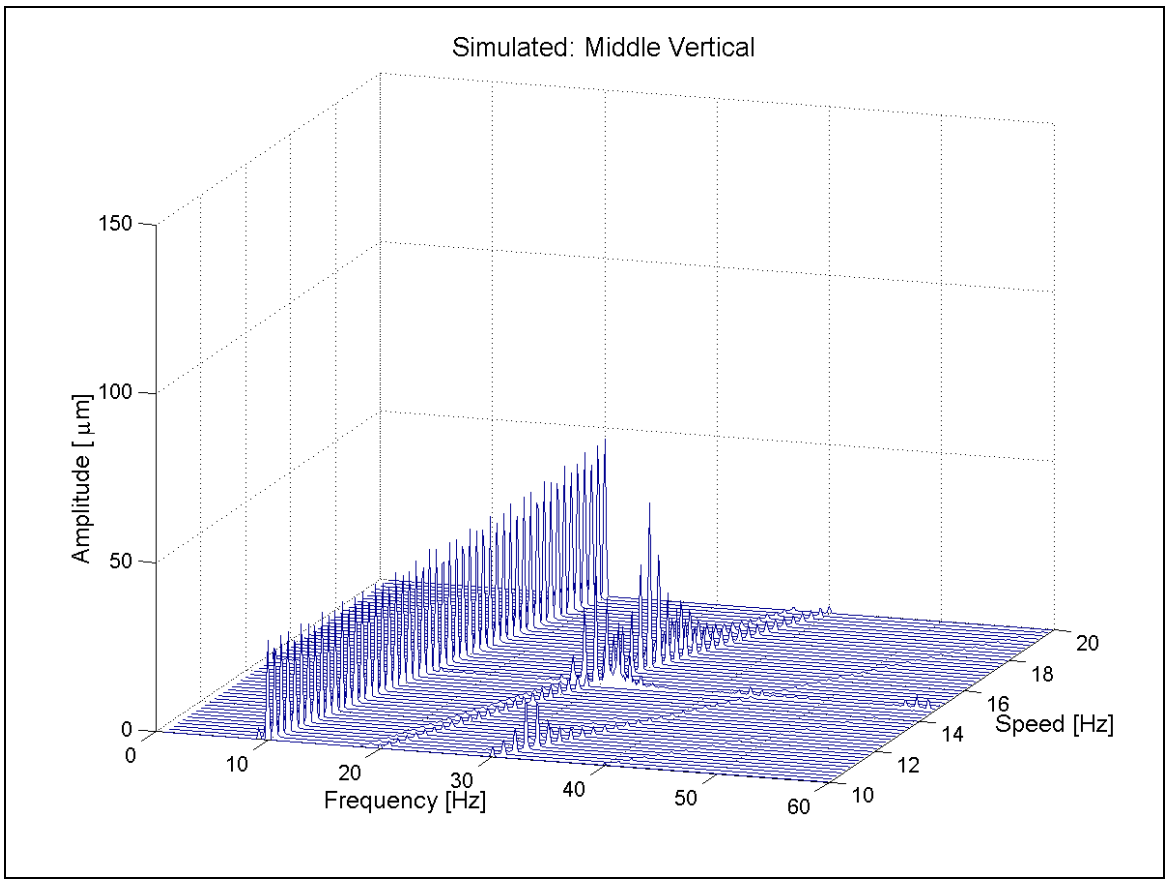

Figure 42. The simulated (CASE 11) spectrum map of vertical throw in the middle of the roll.

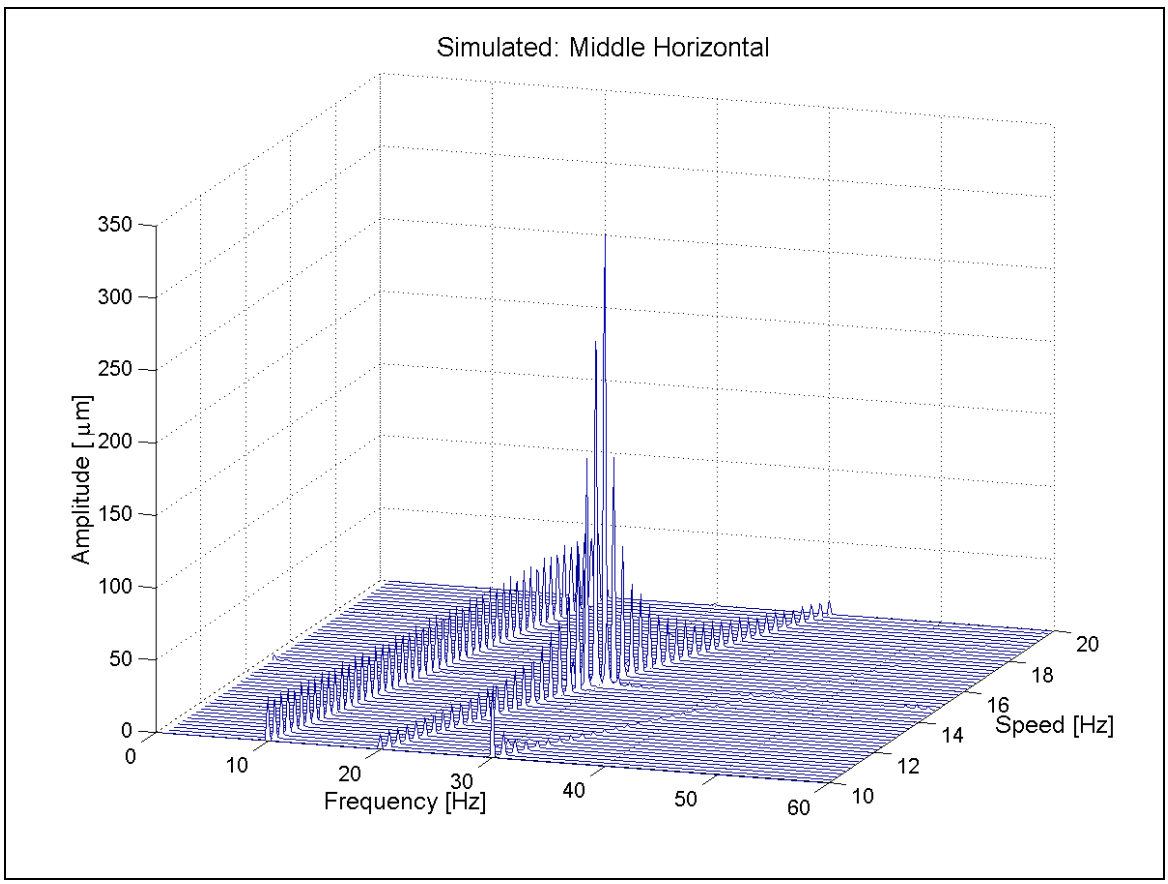

Figure 43. The simulated (CASE 11) spectrum map of horizontal throw in the middle of the roll.

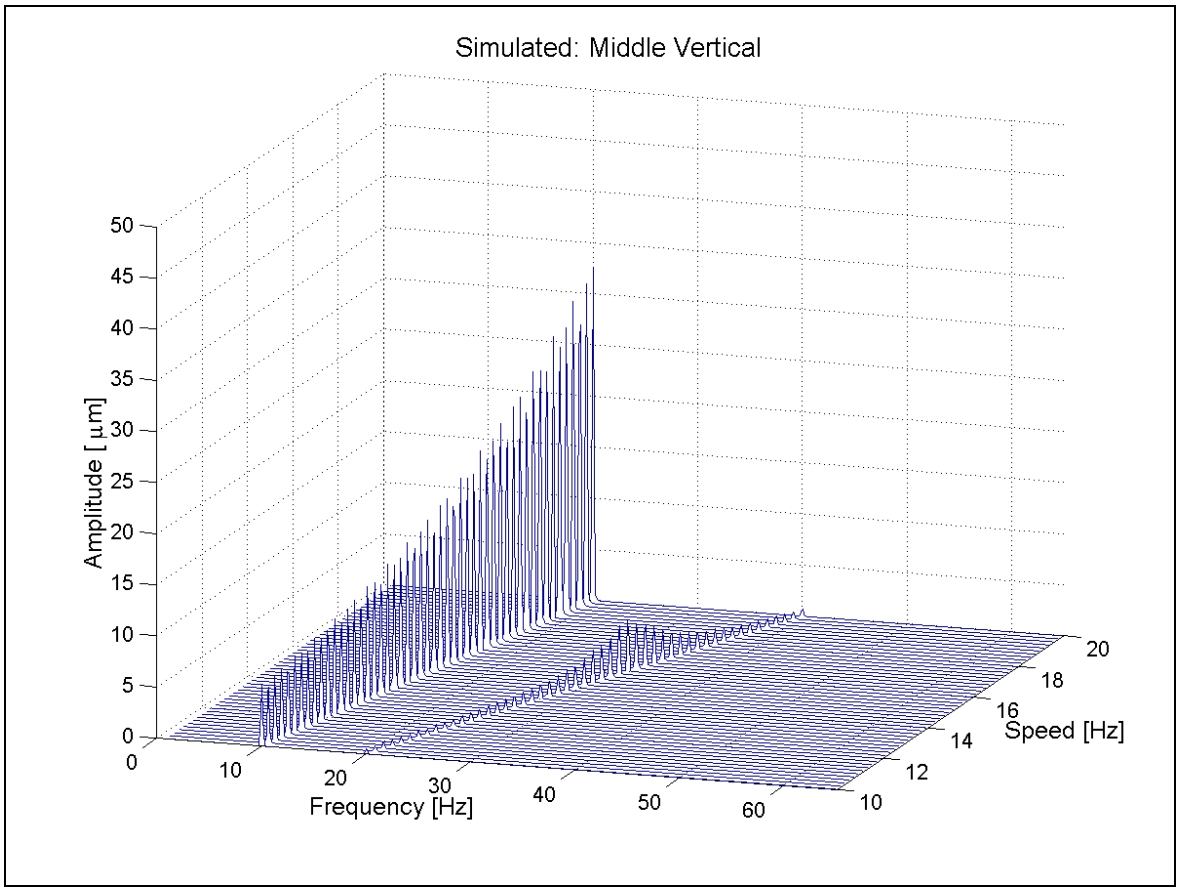

Figure 44. The simulated (CASE 12) spectrum map of vertical throw in the middle of the roll.

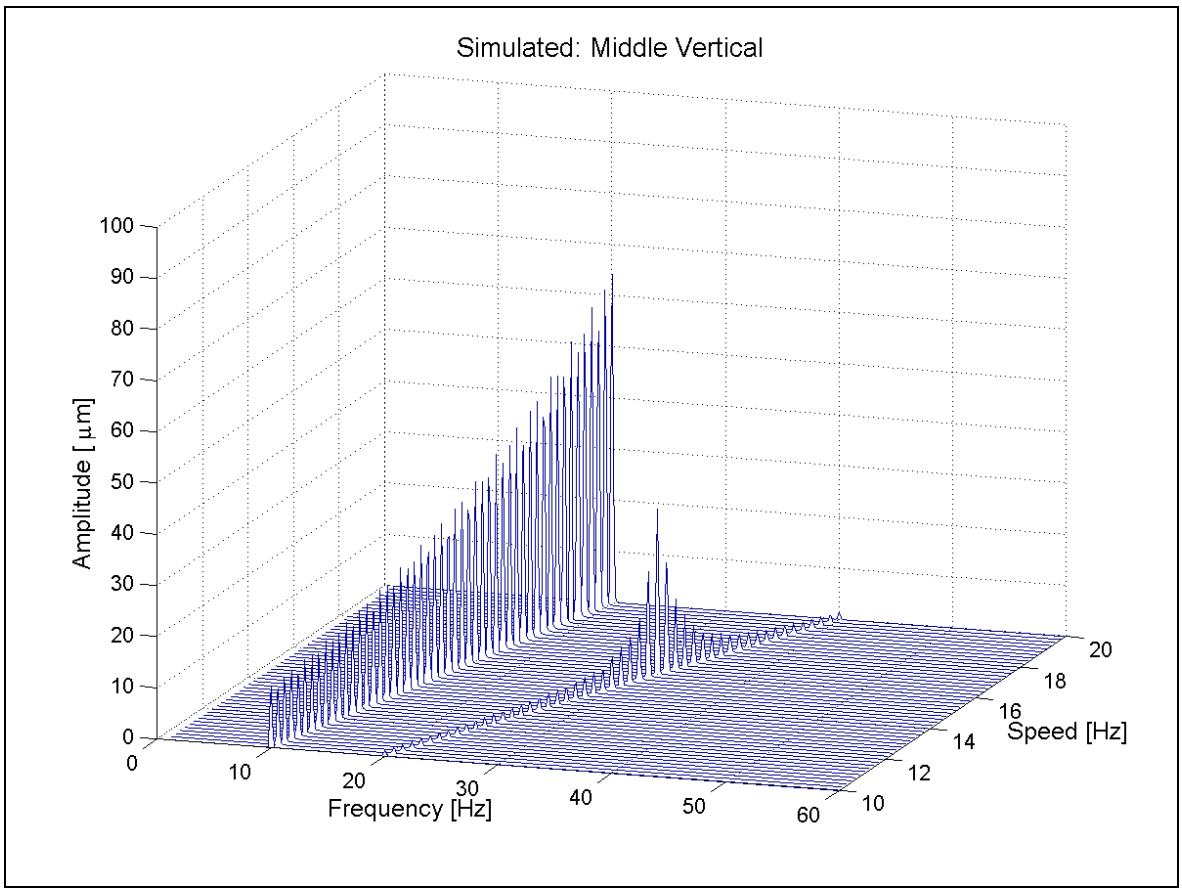

Figure 45. The simulated (CASE 13) spectrum map of vertical throw in the middle of the roll.

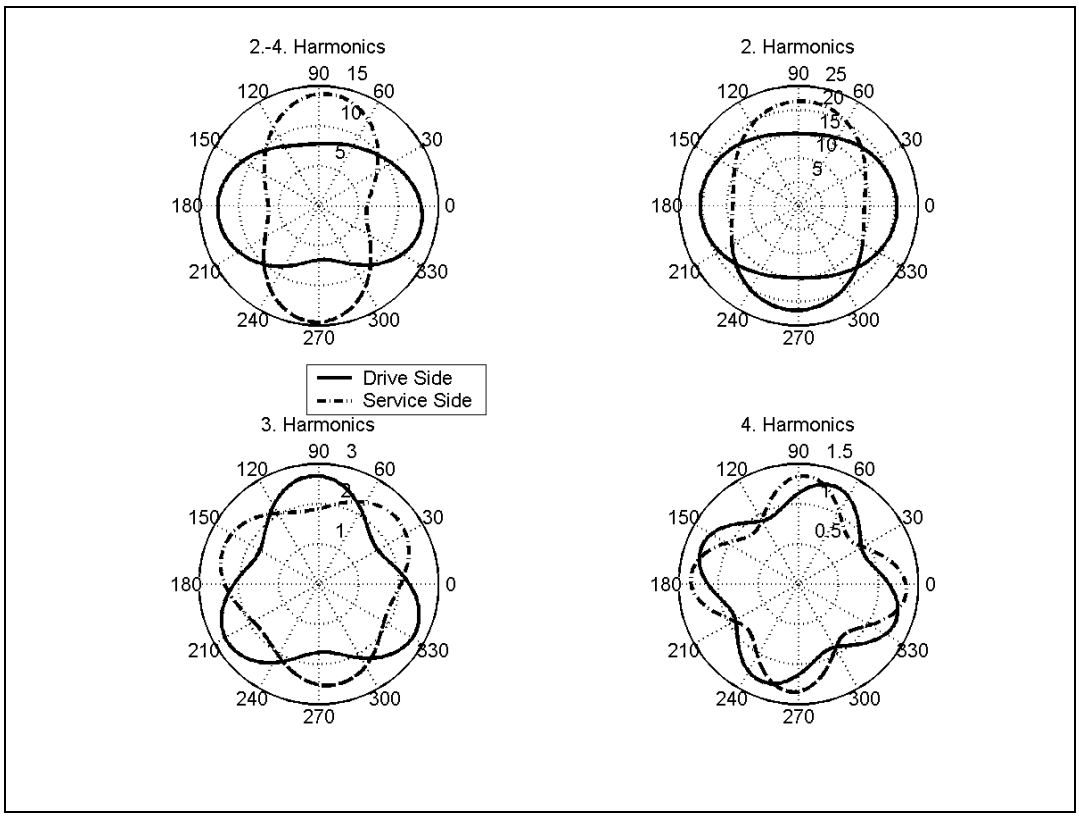

Figure 46. Waviness of the shafts in the CASE 14.

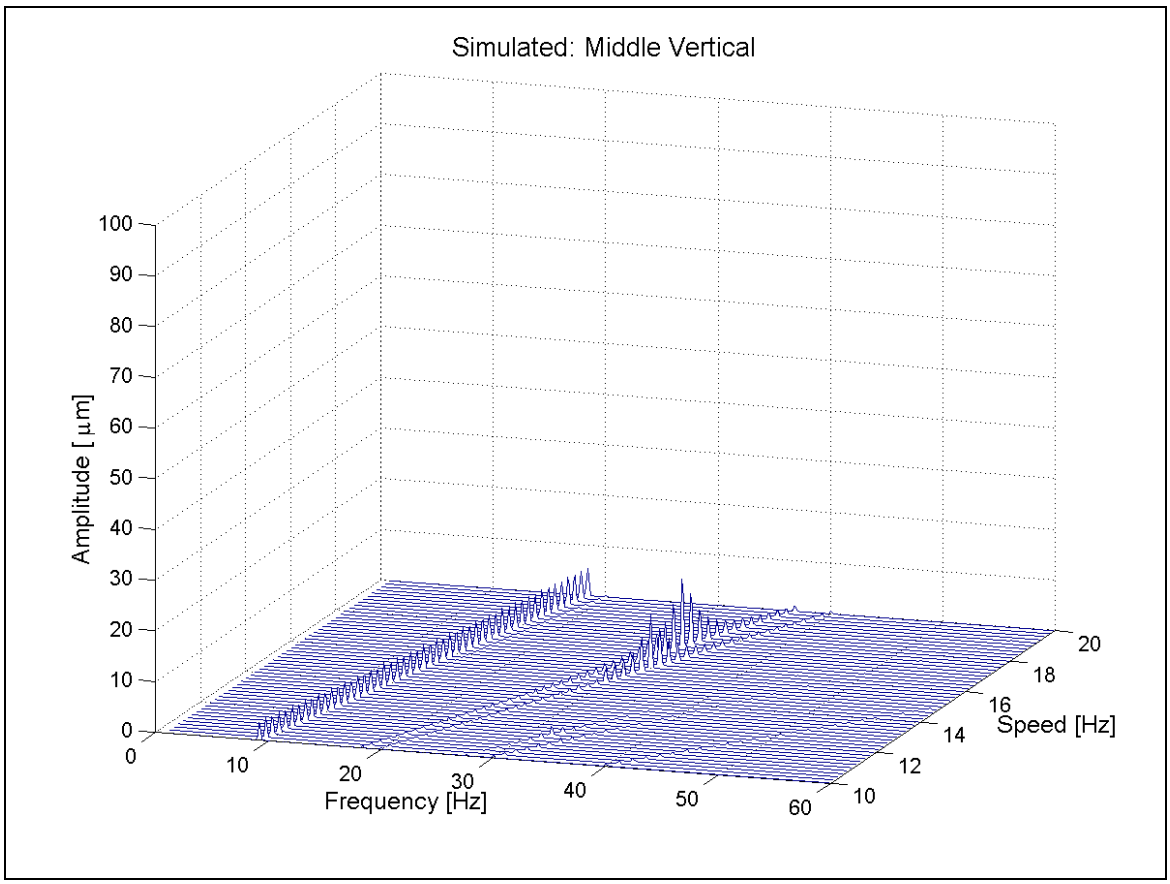

Figure 47. The simulated (CASE 14) spectrum map of vertical throw in the middle of the roll.

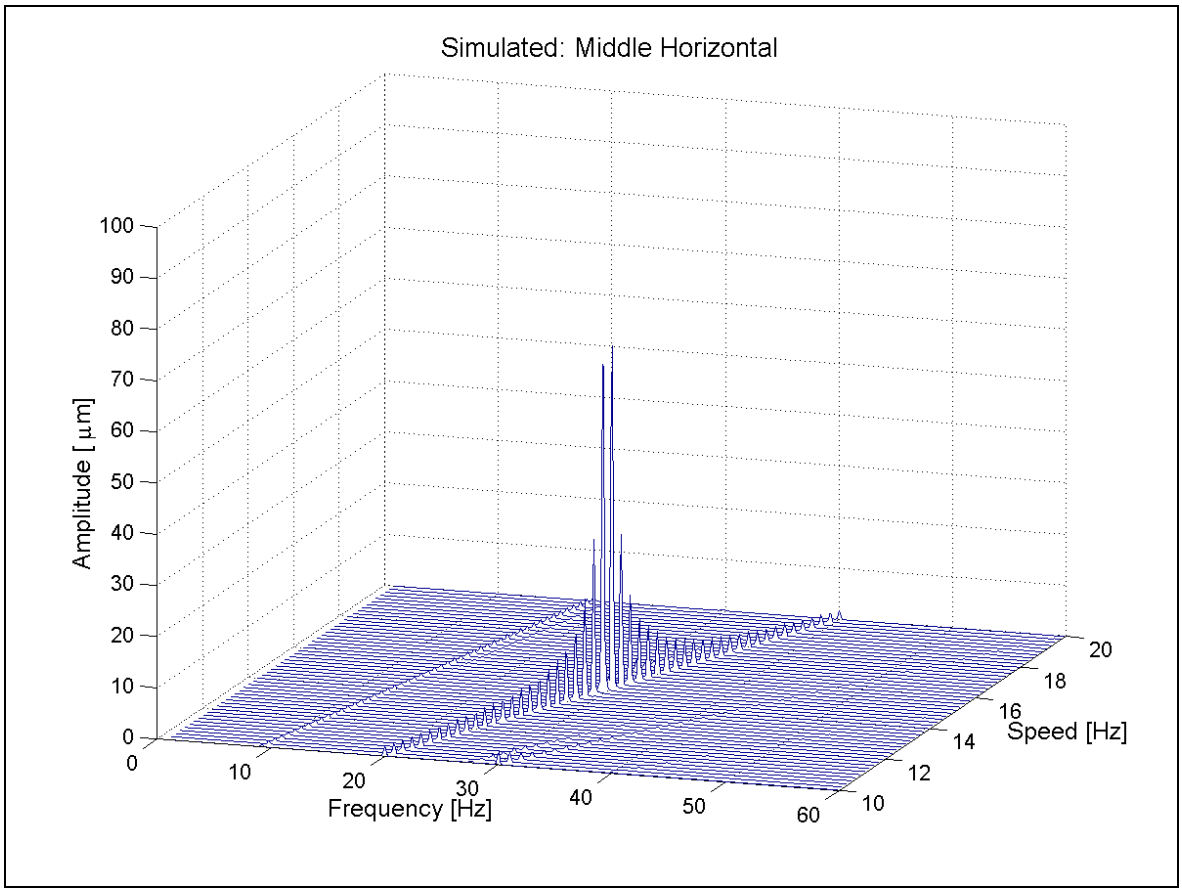

Figure 48. The simulated (CASE 14) spectrum map of horizontal throw in the middle of the roll.

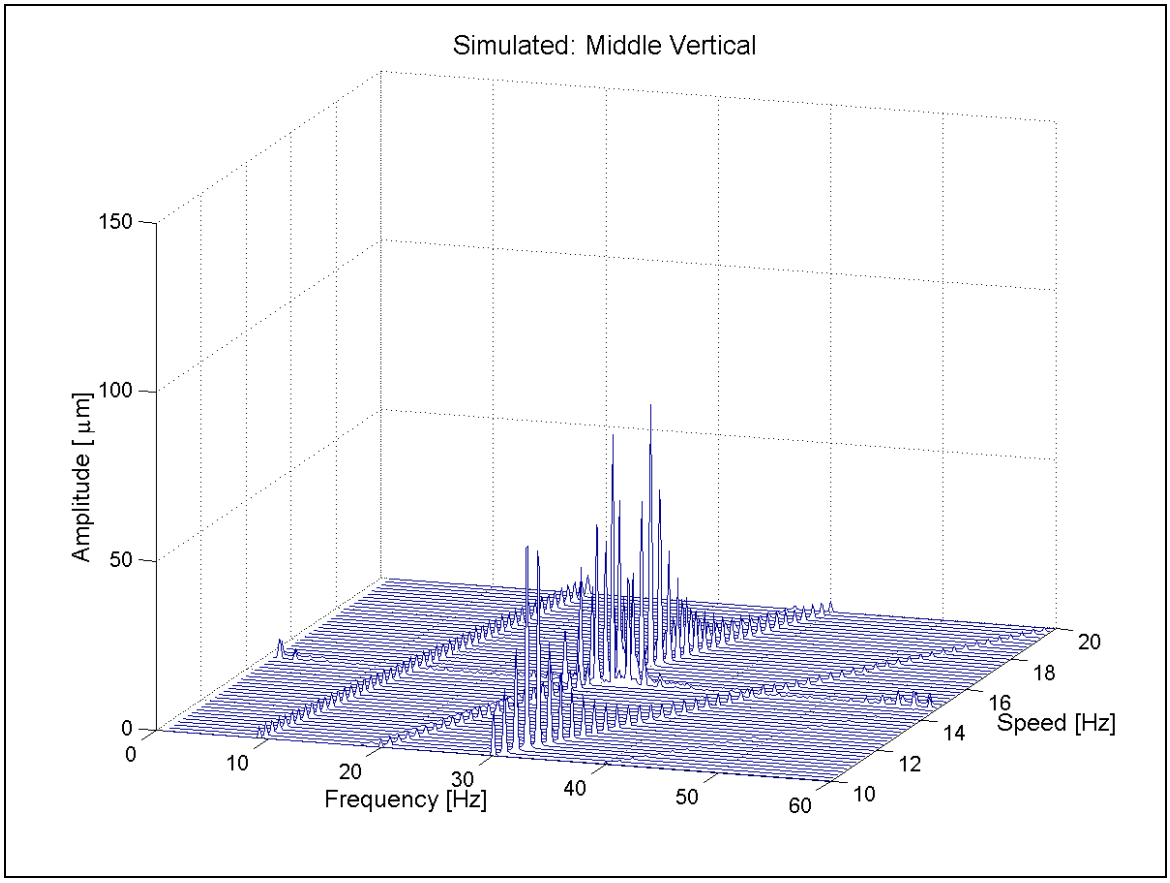

Figure 49. The simulated (CASE 15) spectrum map of vertical throw in the middle of the roll.

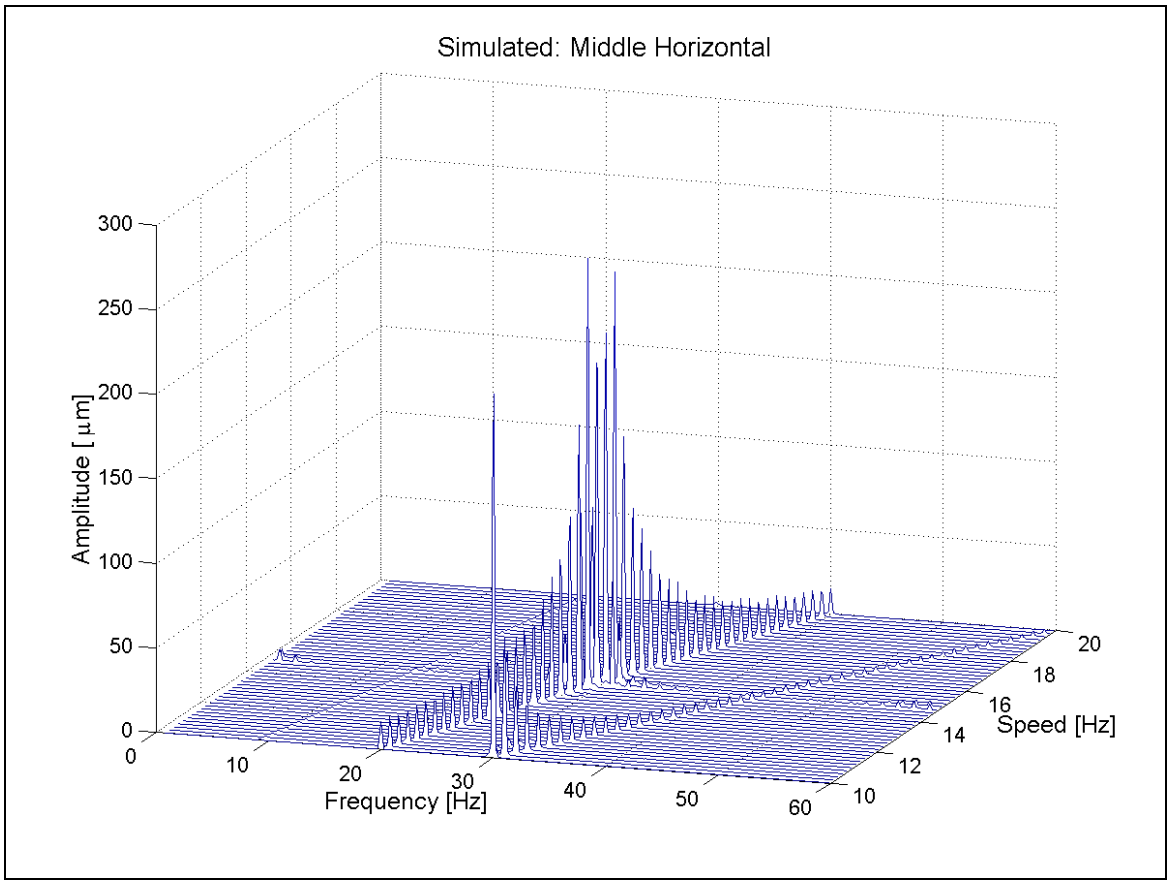

Figure 50. The simulated (CASE 15) spectrum map of horizontal throw in the middle of the roll.

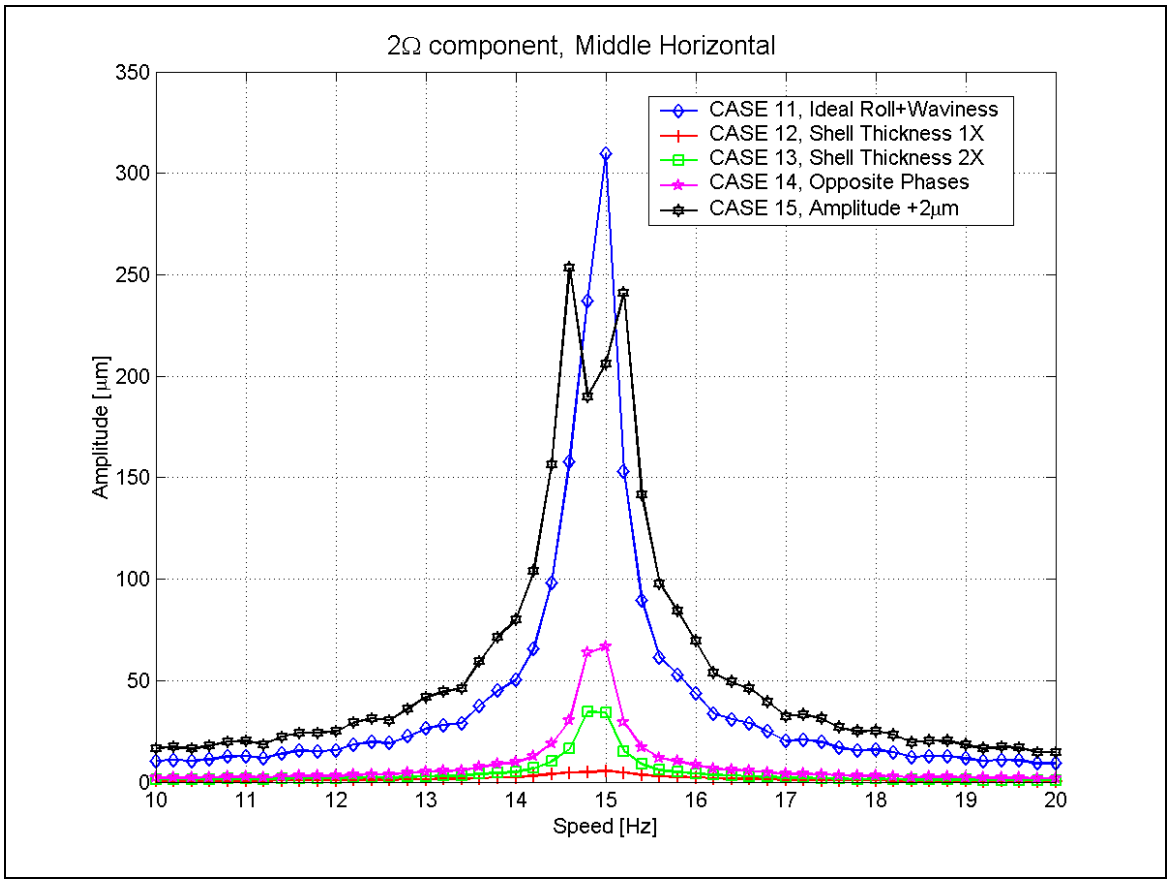

Figure 51. Amplitudes of the horizontal 2nd harmonics at middle in cases 11-15.

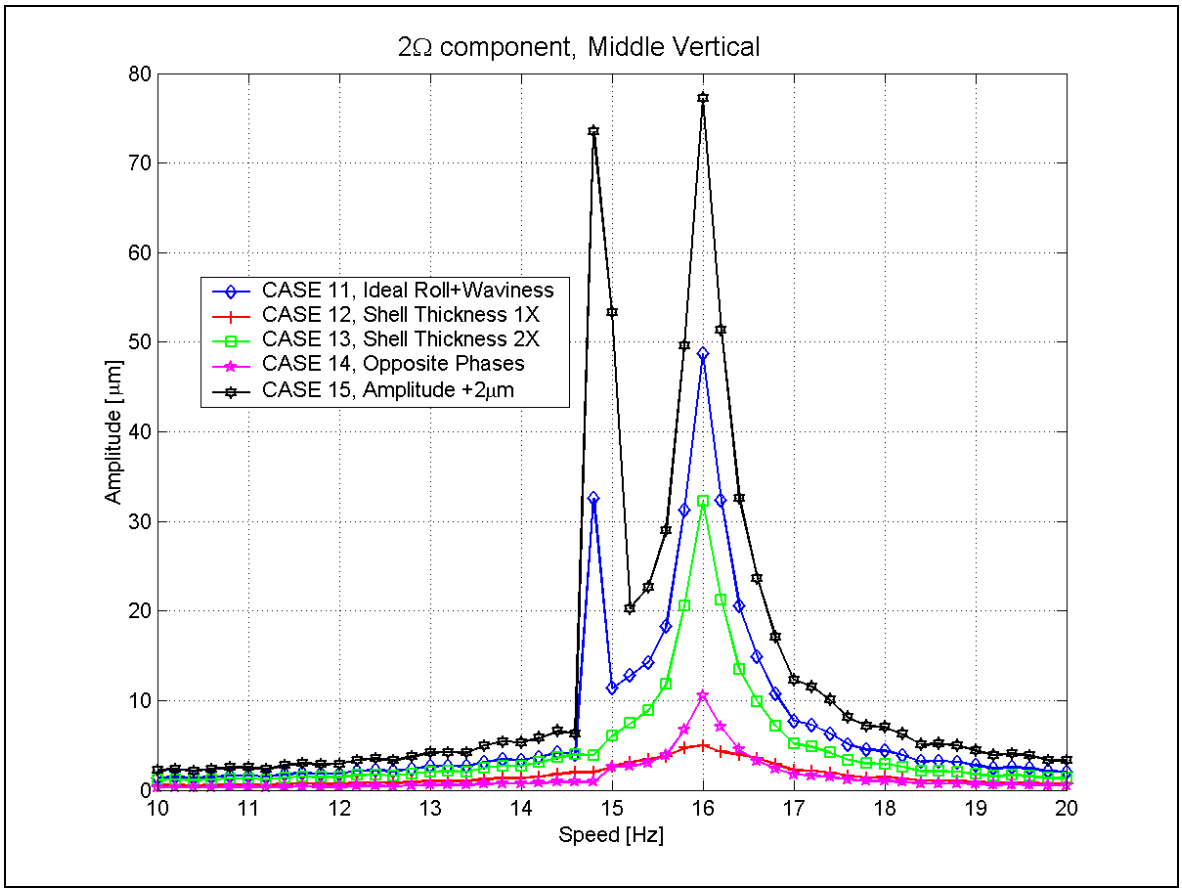

Figure 52. Amplitudes of the vertical 2nd harmonics at middle in cases 11-15.

6.4 CPU-times

Total simulation time in cases 1-7 was 517.4 seconds, which is a relatively long simulation. All the simulations were performed with a stand-alone solver (version 10.0.0 Patch APN-10-55). Error tolerance of the integrator (gear stiff) was 1e-5 and maximum time step size was 2.5e-4 s. All the simulations were performed with Pentium4 1700 MHz processor in the Windows2000 operating system. An average ratio between the CPU-time and the simulated time (Real-Time Ratio) was 204, which means that one spectrum map is calculated in 29 hours. In the CASE 3 this ratio was 183.

An average Real-Time Ratio in the CASE 8 was 823, which was expected because all modes were selected. The increase in CPU-time is not linearly dependent on the number of model degrees of freedom. Degrees of freedom were 2.5 times larger than in the CASE 3 but CPU-time was 4.5 times larger.

As mentioned before, the invariants $\mathbf{I}^5$ and $\mathbf{I}^9$ are computationally expensive. Real-Time Ratio in the CASE 9 ($\mathbf{I}^5$ and $\mathbf{I}^9$ disabled) was 145, where as in the CASE 10 ($\mathbf{I}^9$ disabled) it was 154.

7 CONCLUSIONS

The construction of the ADAMS simulation model of the roller test rig is presented in detail. The flexibility of the parts is imported from detailed FE-models. In ADAMS, the simulation model is assembled and joints as well as forces are defined.

Differential Evolution -optimization algorithm was used to improve the accuracy of the simulation model. The error between the modal parameters in the model and those obtained by experimental modal analysis was minimized. Frequency and modal damping of the 10 vibration modes were used in the optimization. It was shown that DE-algorithm is suitable for this kind of multi-parameter nonlinear optimization.

The modeled non-idealities were shell thickness variation of the roll and roundness errors i.e. waviness of the shafts of the roll. It was proven with the simulation model that the subharmonic resonances are due to these non-idealities. Shell thickness variation causes the weight resonance, which means that symmetrical modes are excited at rotational frequencies $2f$, where f is the frequency of the symmetrical mode. Waviness of the shafts causes subharmonic resonances of order 2Ω, 3Ω, 4Ω, …, $N\Omega$.

In this study, the shell thickness variation of the real roll was measured and modeled in the FE-model. Thus the bending stiffness variation of the roll in the simulation model was due to shell thickness variation only. It seems that the stiffness variation in the real roll is greater, which means that shell thickness is not the only non-ideality of the roll. There can be other non-idealities in the real roll, such as uneven modulus of elasticity or welds, which affect to the stiffness variation. However, measurement of the rolls geometry is not necessary, percentage variation of the bending stiffness can be used instead. Two different variation percentages were used in the simulations, namely 0.33 % and 0.67 %.

The simulation results were compared to those obtained by measuring the real structure. Comparison shows that very good accuracy is achieved. The half critical subharmonic resonance was studied in detail. Vibration responses are due to very small non-idealities in the real structure and these non-idealities are difficult or even impossible to measure. Several simulation cases were run where values of the initial parameters were varied. These variations were within the error estimates of the measured data. The simulation results show that equivalent responces are achieved within the error limit of the initial parameters. It can be said that the simulation model can predict the responses of the half-critical resonances accurately.

REFERENCES

[1] Uski, T., Juhanko, J., 2000, "Initial curvature measurement of the test roll (In Finnish)", Helsinki University of Technology Reports in Machine Design 8/2000, Measurement report, 22 p.

[2] ANSYS Theory Reference, 1999, Eleventh Edition, SAS IP, Inc. ©.

[3] Sopanen, J., Mikkola, A., 2000, Study of sub-harmonic vibration of a tube roll using simulation model. 2nd Triennial International Symposium on Multi-body Dynamics: Monitoring & Simulation Techniques, Bradford, UK.

[4] Óttarsson, G., 2000, Modal Flexibility Method in ADAMS/FLEX. MDI Technical Paper, Available at: http://support.adams.com/kb/faq.asp?ID=kb7247.dasp.

[5] Craig, R. R., Bampton, M. C. C., 1968, Coupling of Substructures for Dynamic Analyses, AIAA Journal, Vol. 6, No. 7, pp. 1313-1319.

[6] Kantola, K., 2000, "Modal analysis of the test roll (In Finnish)", Measurement report, Helsinki University of Technology, Laboratory of Mechanics of Materials, 16 p.

[7] Hamrock, B. J., 1994, Fundamentals of Fluid Film Lubrication. McGraw-Hill, New York.

[8] ADAMS 10.0 Online Documentation, 1999, Mechanical Dynamics, Inc.

[9] Eschmann, P., 1986, Ball and Roller Bearings, Theory, Design and Application, 2nd edition, John Wiley and Sons, New York.

[10] Krämer, E., 1993, Dynamics of Rotors and Foundation, Spinger-Verlag, Berlin.

[11] Sohoni, W. E. and Whitesell, J., 1986, "Automatic Linearization of Constrained Dynamical Models", *Journal of Mechanisms, Transmission an Automation in Design*, **108**, pp. 300-304.

[12] Lampinen, J., 1999, *Differential Evolution – New Naturally Parallel Approach for Engineering Design Optimization*. In: Barry H.V. Topping (ed.), 1999, Developments in Computational Mechanics with High Performance Computing, Civil-Comp Press, Edinburgh (Scotland), pp. 217-228.

[13] Storn, R. and Price, K., 1995. *Differential Evolution - a Simple and Efficient Adaptive Scheme for Global Optimization over Continuous Spaces*. Technical Report TR-95-012, ICSI, March 1995.

[14] Juhanko, J. and Porkka, E., 2001, "PyöriVÄRE – Verification measurement of the roller test rig, balancing machine support", Helsinki University of Technology Reports in Machine Design 2/2001.

APPENDIX I. The functioning of DE is here illustrated in case of a simple objective function $f(X) = x_1 + x_2 + x_3 + x_4 + x_5$. [12]

Differential Evolution (DE)

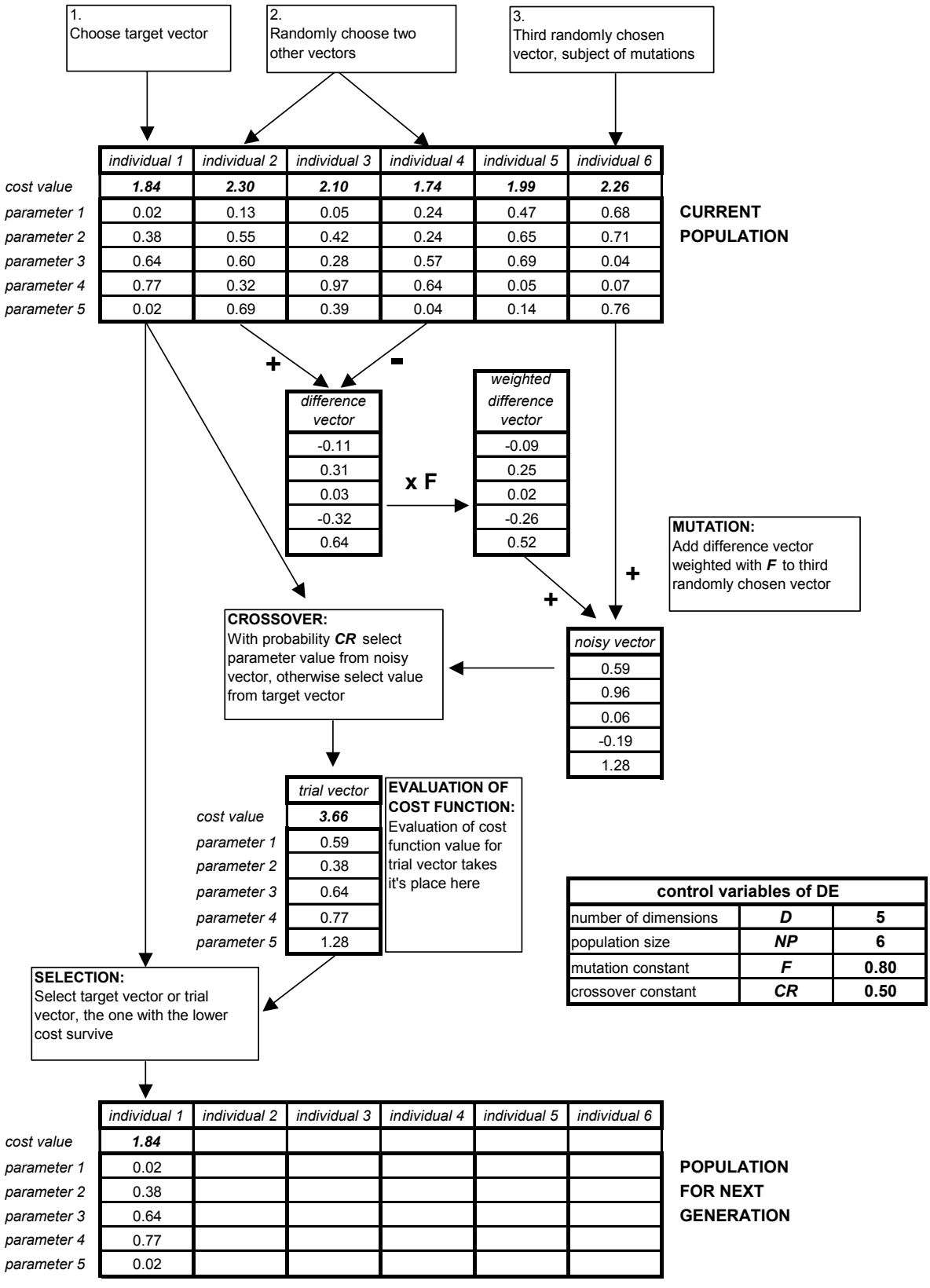

APPENDIX II. The user interface of the Optimize –program.

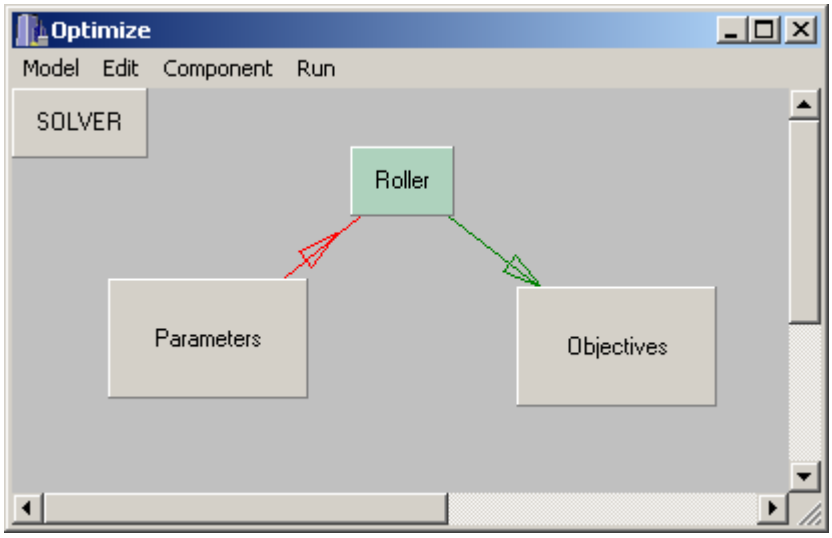

Figure II.1. The model-building environment in Optimize -program. Roller –block is the ADAMS model, which reads in the parameters and return the value of the target function.

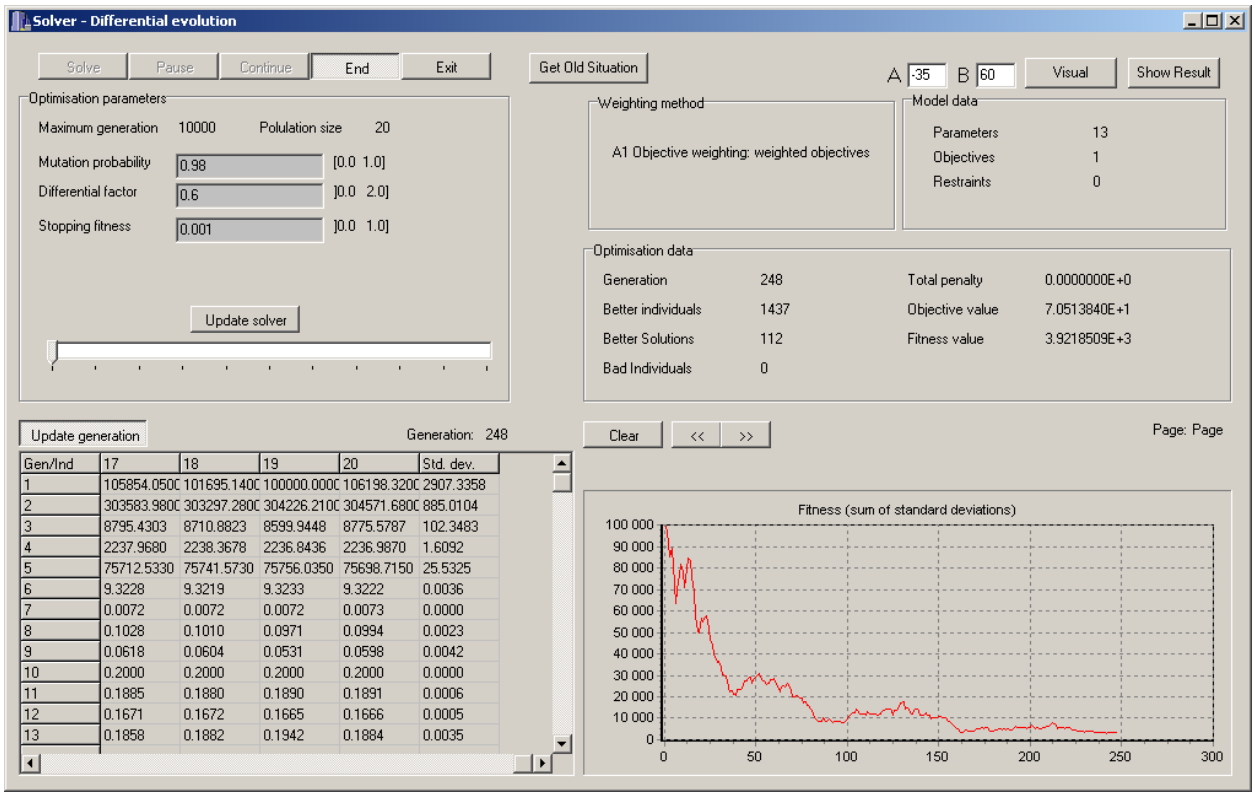

Figure II.2. The solver window of the Optimize program. Sum of standard deviations of parameters is used as a measure of fitness.

APPENDIX III. Optimization results used in the simulation CASE 4.

Table III.1. Optimization results.

Mode	Measured		Simulated								Weight. factor	Target function (absolute error)	
			Before Optimization				After Optimization						
	Damp. %	Freq. [Hz]	Damp. %	Error %	Freq. [Hz]	Error %	Damp. %	Error %	Freq. [Hz]	Error %	C	Before	After
1 (h)	**0.608**	**29.83**	0.344	43.4%	29.43	1.4%	**0.556**	**8.6%**	29.79	0.1%	10	30.432	0.420
2 (v)	**0.900**	**32.16**	0.286	68.2%	32.02	0.4%	**0.901**	**-0.1%**	32.03	0.4%	10	62.841	1.331
3 (h)	**1.330**	**65.34**	1.515	-13.9%	63.79	2.4%	**1.361**	**-2.3%**	65.46	-0.2%	5	16.977	0.613
4 (v)	**1.680**	**82.23**	1.406	16.3%	79.95	2.8%	**1.845**	**-9.8%**	80.88	1.6%	2	10.034	2.698
5 (h)	**1.590**	**111.59**	1.893	-19.1%	108.43	2.8%	**1.731**	**-8.9%**	110.58	0.9%	5	30.963	5.025
6 (v)	**1.850**	**140.00**	1.553	16.1%	138.82	0.8%	1.382	25.3%	140.01	0.0%	2	8.300	9.375
7 (h)	**2.100**	**179.04**	**1.927**	**8.2%**	182.40	-1.9%	**2.246**	**-7.0%**	184.75	-3.2%	1.25	4.201	7.132
8 (h)	**2.030**	**206.62**	1.413	30.4%	224.18	-8.5%	**1.851**	**8.8%**	225.92	-9.3%	1.25	29.668	24.120
9 (v)	**1.540**	**267.00**	**1.551**	**-0.7%**	258.21	3.3%	**1.414**	**8.2%**	259.15	2.9%	0.625	5.493	4.905
10 (h)	**1.120**	**282.78**	0.682	39.1%	307.97	-8.9%	**0.800**	**28.6%**	308.32	-9.0%	0.625	18.481	17.960
h = horizontal mode			**Mean:**	**25.5%**	**Mean:**	**3.3%**	**Mean:**	**10.8%**	**Mean:**	**2.8%**	**Sum:**	**217.39**	**73.58**
v = vertical mode											**Improvement:**		**66.2%**

Table III.2. Optimized parameters.

Parameter	Range		Initial value	Optimal Value	Units
	min	max			
DV_1_KX_ground	100.00	2500.00	700.00	119.74	MN/m
DV_2_KY_ground	100.00	2500.00	700.00	410.20	MN/m
DV_3_CX_ground	1.00	100000.00	1000.00	9673.37	Ns/mm
DV_4_CY_ground	1.00	100000.00	1000.00	1960.04	Ns/mm
DV_5_K_piezo	60.00	80.00	70.00	73.93	MN/m
DV_6_C_piezo	1.00	100.00	5.00	8.52	Ns/mm
DV_7_c1_roll	0.01	10.00	0.50	0.45	%
DV_8_c1_frame	0.05	20.00	0.50	3.99	%
DV_9_c2_frame	0.05	20.00	0.50	19.72	%
DV_10_c3_frame	0.05	20.00	0.50	19.78	%
DV_11_c1_stpl	0.05	20.00	0.50	19.56	%
DV_12_c2_stpl	0.05	20.00	0.50	0.63	%
DV_13_c3_stpl	0.05	20.00	0.50	18.04	%